Aerosol Effects on Clear-Sky Shortwave Heating in the Asian Monsoon Tropopause Layer

Jie Gao[1], Yi Huang[2], Yiran Peng[1], and Jonathon S. Wright[1]

[1]Tsinghua University
[2]McGill University

November 23, 2022

Abstract

The Asian Tropopause Aerosol Layer (ATAL) has emerged in recent decades to play a prominent role in the upper troposphere and lower stratosphere above the Asian monsoon. Although ATAL effects on surface and top-of-atmosphere radiation budgets are well established, the magnitude and variability of ATAL effects on radiative transfer within the tropopause layer remain poorly constrained. Here, we investigate the impacts of various aerosol types and layer structures on clear-sky shortwave radiative heating in the Asian monsoon tropopause layer using reanalysis products and offline radiative transfer simulations. ATAL effects on shortwave radiative heating based on the MERRA-2 aerosol reanalysis are on the order of 10% of mean clear-sky radiative heating within the tropopause layer, although discrepancies among recent reanalysis and forecast products suggest that this ratio could be as small as ˜5% or as large as ˜25%. Uncertainties in surface and top-of-atmosphere flux effects are also large, with values spanning one order of magnitude at the top-of-atmosphere. ATAL effects on radiative heating peak between 150 hPa and 80 hPa (360 K–400 K potential temperature) along the southern flank of the anticyclone. Clear-sky and all-sky shortwave heating are at local minima in this vertical range, which is situated between the positive influences of monsoon-enhanced water vapor and the negative influence of the 'ozone valley' in the monsoon lower stratosphere. ATAL effects also extend further toward the west, where diabatic vertical velocities remain upward despite descent in pressure coordinates.

Aerosol Effects on Clear-Sky Shortwave Heating in the Asian Monsoon Tropopause Layer

Jie Gao[1], Yi Huang[2], Yiran Peng[1], and Jonathon S. Wright[1]

[1]Department of Earth System Science, Ministry of Education Key Laboratory for Earth System Modeling, and Institute for Global Change Studies, Tsinghua University, Beijing, China

[2]Department of Atmospheric and Oceanic Sciences, McGill University, Montreal, Quebec, Canada

Key Points:

- The Asian tropopause aerosol layer produces a 5–25% direct enhancement of clear-sky shortwave heating above the summer monsoon
- Effects are largest where shortwave heating is weakest, with similar magnitudes to water vapor and ozone effects near the monsoon tropopause
- Discrepancies across recent aerosol analysis and forecast products cause large uncertainties in aerosol forcing of heating and fluxes

Corresponding author: Jonathon S. Wright, jswright@tsinghua.edu.cn

Abstract

The Asian Tropopause Aerosol Layer (ATAL) has emerged in recent decades to play a prominent role in the upper troposphere and lower stratosphere above the Asian monsoon. Although ATAL effects on surface and top-of-atmosphere radiation budgets are well established, the magnitude and variability of ATAL effects on radiative transfer within the tropopause layer remain poorly constrained. Here, we investigate the impacts of various aerosol types and layer structures on clear-sky shortwave radiative heating in the Asian monsoon tropopause layer using reanalysis products and offline radiative transfer simulations. ATAL effects on shortwave radiative heating based on the MERRA-2 aerosol reanalysis are on the order of 10% of mean clear-sky radiative heating within the tropopause layer, although discrepancies among recent reanalysis and forecast products suggest that this ratio could be as small as ∼5% or as large as ∼25%. Uncertainties in surface and top-of-atmosphere flux effects are also large, with values spanning one order of magnitude at the top-of-atmosphere. ATAL effects on radiative heating peak between 150 hPa and 80 hPa (360 K–400 K potential temperature) along the southern flank of the anticyclone. Clear-sky and all-sky shortwave heating are at local minima in this vertical range, which is situated between the positive influences of monsoon-enhanced water vapor and the negative influence of the 'ozone valley' in the monsoon lower stratosphere. ATAL effects also extend further toward the west, where diabatic vertical velocities remain upward despite descent in pressure coordinates.

Plain Language Summary

Every summer, a layer of polluted air laden with aerosol particles collects above the convective storms of the Asian monsoon as part of a broad upper-level circulation centered over the Tibetan Plateau. Researchers have developed a working understanding of how the dynamical environment shapes this Asian tropopause aerosol layer. The motivating question for this work is: how might the aerosol layer reshape its environment? Aerosols can absorb and scatter sunlight, affecting both the amount of sunlight transmitted through the layer and the magnitude of solar heating within the layer. These effects depend on aerosol species and their vertical distribution within the layer, both of which are highly variable. In this paper, we translate variations and uncertainties in the amount, composition, and vertical distribution of aerosols near the Asian monsoon tropopause into variations and uncertainties in the absorption and scattering of solar radiation by the aerosol layer. We find that aerosols account for a substantial part (5-25%) of heating by solar radiation near the tropopause. The vertical location and horizontal extent of the aerosol effects are distinct from those of other radiative effects.

1 Introduction

Aerosol effects on radiative heating are among the most uncertain and complex challenges to understanding atmospheric variability at scales ranging from the development of weather systems to the long-term evolution of climate (Ramaswamy et al., 2018; Szopa et al., 2021). Different aerosol types have different direct effects on atmospheric radiative transfer. Direct effects, also referred to as radiative forcing from aerosol–radiation interactions, can be broadly classified into absorption and scattering by atmospheric aerosols. For example, black carbon (BC), brown carbon (a form of organic carbon; OC), and some mineral dust particles can directly absorb solar radiation (K.-M. Lau & Kim, 2006; Samset et al., 2018), while sulfate, nitrate, and most dust and OC aerosols act mainly to scatter solar radiation (Whitby, 1978; Kinne et al., 2006). In addition to these direct effects, indirect radiative effects include, for example, aerosol-induced changes in the occurrence frequencies, lifetimes, and optical properties of clouds (Twomey, 1977; Albrecht, 1989; Lohmann, 2017; Kreidenweis et al., 2019). As a general rule, and with the exception of very large aerosol particles, direct forcing by aerosol–radiation interactions mainly in-

fluences the shortwave (solar) part of the spectrum, while indirect effects influence both longwave (thermal) and shortwave radiative transfer (Charlson et al., 1992).

Aerosol distributions are highly variable in space and time owing to spatial gradients in emissions, secondary formation processes, and spatiotemporal heterogeneity in the efficiency of removal processes (Kreidenweis et al., 2019). The prevalence of internal mixing and large uncertainties in aerosol optical properties further complicate the identification of aerosol types and their impacts on atmospheric radiation. As a consequence, there remain substantial uncertainties in the magnitude of direct aerosol radiative forcings at the surface and top-of-atmosphere (Ramaswamy et al., 2018; Kuniyal & Guleria, 2018; Szopa et al., 2021), let alone in the vertical profile of radiative heating. These challenges are especially acute with respect to the structure and radiative effects of the Asian tropopause aerosol layer (ATAL; Vernier et al., 2011), which develops each year during boreal summer in the upper troposphere and lower stratosphere (UTLS) above the Asian summer monsoon (Vernier et al., 2015; Yu et al., 2015; Bian et al., 2020).

The Asian summer monsoon is among the most important sources of water vapor and tropospheric pollutants to the global stratosphere (Fu et al., 2006; Randel et al., 2010; Pan et al., 2016; Ploeger et al., 2017; Yu et al., 2017; Lelieveld et al., 2018). Strong deep convection associated with the monsoon pumps moist, polluted air (Park et al., 2007; Pan et al., 2016; Bian et al., 2020) upward into a vigorous upper-level anticyclone bounded by the tropical easterly jet to the south and the subtropical westerly jet to the north (Hoskins & Rodwell, 1995; Garny & Randel, 2013; Legras & Bucci, 2020). Much of the air within this upper-level monsoon anticyclone traces back to the boundary layer over South and East Asia (Bergman et al., 2013; Orbe et al., 2015; Vogel et al., 2016; Zhang et al., 2020), where abundant emissions of aerosols and aerosol precursors contribute to ATAL formation (Neely et al., 2014; Yu et al., 2015; Vernier et al., 2017; Bian et al., 2020). Enhanced aerosol concentrations in the UTLS alter radiative heating at the tropopause level both directly (Toohey et al., 2014; Vernier et al., 2015; Yu et al., 2015; Fadnavis et al., 2017, 2019) and indirectly through their interactions with clouds (Su et al., 2011; Dong et al., 2019; Fadnavis et al., 2019). However, the practical impacts of these aerosol effects depend in large part on the composition and vertical structure of the aerosol layer, which are highly variable (Hanumanthu et al., 2020) and poorly constrained (Bian et al., 2020).

Estimates of ATAL composition are based mainly on numerical models, some of which indicate that sulfate aerosols originating from East Asia are the leading component (Neely et al., 2014; Vernier et al., 2015; Yu et al., 2015), while others point to nitrate aerosols (Gu et al., 2016) and still others point to leading roles for organic aerosols or dust (W. K. M. Lau et al., 2018; Ma et al., 2019; Bossolasco et al., 2021). Observational studies conducted on ATAL composition to date do not support large concentrations of dust at the tropopause level (Vernier et al., 2017) and highlight a surprising abundance of nitrate aerosols (Höpfner et al., 2019), which are still not represented in many models (Kreidenweis et al., 2019; Bossolasco et al., 2021). Other observational studies, while unable to measure aerosol composition, have emphasized large variations in ATAL amplitude and vertical structure at daily time scales (Brunamonti et al., 2018; Zhang et al., 2020; Hanumanthu et al., 2020; Mahnke et al., 2021). These variations and associated uncertainties complicate efforts to constrain the radiative effects of the ATAL.

The ATAL is distinct from episodic volcanic aerosol loading of the lower stratosphere in its composition, seasonality, vertical location, and longitudinal extent (Bian et al., 2020). Although much progress has been made in evaluating the variability, formation mechanisms, and tropospheric sources of the ATAL, its effects on the energy budget and thermodynamic structure of the tropopause layer are not yet clear. Important steps in this direction include the model-based analyses conducted by Yu et al. (2015) and Fadnavis et al. (2017, 2019), along with a recent reanalysis-based dynamical assessment of ATAL evolution as observed by satellite (He et al., 2021). However, given inter-model discrepancies and observational uncertainties in the composition and structure of the ATAL,

the extent to which the results of these studies can be generalized to other model systems or the natural atmosphere remains unclear.

As a step toward addressing this gap, we adopt an idealized framework to examine ATAL effects on radiative heating in the monsoon UTLS, focusing on clear-sky shortwave heating. We focus on shortwave effects for three reasons. First, aerosol radiative forcing are mainly confined to the shortwave part of the spectrum, especially for the relatively small aerosol particles that predominate within the ATAL (Vernier et al., 2017; Mahnke et al., 2021; Weigel et al., 2021). Second, the shortwave effects of aerosol perturbations in the UTLS can be treated as a diabatic forcing while longwave responses are often dominated by thermal relaxation (Toohey et al., 2014). Third, convective ventilation of the UTLS above the monsoon also creates regional-scale anomalies in ozone and water vapor, both of which play important roles in shortwave radiative transfer near the tropopause. These anomalies provide convenient comparison points for evaluating the relative influences of ATAL on shortwave heating in the UTLS. Further restricting our analysis to clear-sky conditions is motivated mainly by the ATAL being located above the majority of convective anvil clouds (Vernier et al., 2015; Bian et al., 2020). Although aerosols also have important impacts on the frequency, distribution, and optical properties of tropopause-level cirrus clouds (Su et al., 2011; Riuttanen et al., 2016; Fadnavis et al., 2019), these interactions are poorly constrained. Accounting for aerosol effects on cirrus clouds would thus compound already large uncertainties while requiring evaluation of aerosol–cloud covariability, and is deferred to future work.

This paper is organized in five parts. In Section 2, we introduce the reanalysis and forecast products and the libRadtran radiative transfer model. In Section 3, we examine the spatial and temporal distributions of aerosol in the Asian monsoon UTLS according to the MERRA-2 reanalysis and describe a series of idealized sensitivity experiments exploring the clear-sky shortwave effects of variations in the amplitude, composition, and vertical structure of the ATAL. In Section 4, we contextualize the ATAL radiative effects by comparing their magnitudes and distributions to those of ozone, water vapor, and clouds, as well as quantifying the impacts of uncertainties in ATAL composition and structure across recent reanalysis and forecast products. In Section 5, we provide a short summary of the conclusions and possible next steps.

2 Data and Methods

2.1 The MERRA-2 aerosol reanalysis

The primary dataset for this study is the Modern-Era Retrospective Analysis for Research and Applications, version 2 (MERRA-2; Gelaro et al., 2017) for the 10-year period 2011–2020. MERRA-2 is unique among current meteorological reanalyses (see Wright et al., 2022, their Table 2.12) in that it includes an interactive aerosol analysis (Randles et al., 2017). Aerosols are simulated via the Goddard Chemistry, Aerosol, Radiation, and Transport (GOCART) model, which considers sources, sinks, and chemical properties of 15 aerosol types and classes, including dust (five non-interacting size bins), sea salt (five non-interacting size bins), sulfate, hydrophilic and hydrophobic BC, and hydrophilic and hydrophobic OC (Chin et al., 2002; P. Colarco et al., 2010; P. R. Colarco et al., 2014; Randles et al., 2017). Observations used in the data assimilation are limited to remote sensing measurements of aerosol optical depth (AOD) and do not alter the composition or relative vertical distribution of aerosols (Randles et al., 2017).

Although prescribed emissions to the aerosol model vary in time over much of the 1980–2010 period, most emissions sources use either constant or annually-repeating monthly values over the analysis period 2011–2020 (Randles et al., 2017). This includes volcanic emissions, which only include a repeating annual cycle of outgassing (omitting eruptions) after 2010. Injections of sulfate to the stratosphere by volcanic eruptions can make it dif-

ficult to distinguish the ATAL (Thomason & Vernier, 2013; Vernier et al., 2015). Limiting our analysis to 2011–2020 essentially eliminates this potential confounding effect. Biomass burning emissions are from version 2.4 of the Quick Fire Emissions Database (QFED; Darmenov & da Silva, 2015). MERRA-2 has been shown to perform well with respect to independent observations of AOD and fluxes (Randles et al., 2017), as well as absorbing aerosol optical depth, ultraviolet index, and vertical structure (Buchard et al., 2017). The ATAL in MERRA-2 has previously been examined by W. K. M. Lau et al. (2018), who focused on carbonaceous aerosols and dust during the pre-monsoon and peak monsoon periods (May–August) of 2008. Their results showed that MERRA-2 produces a well-defined ATAL fed mainly by deep convection over North India and the Sichuan Basin. Further details on emissions, previous validation, and the rationale for using MERRA-2 as the basis for this work are provided in Supporting Information (Text S1).

MERRA-2 products used in this work include daily-mean vertical profiles of temperature, specific humidity, mass mixing ratios of ozone and aerosol species, pressure, and geopotential height; temperature tendencies due to clear-sky radiative heating on model levels for the analysis window 04:30–07:30 UTC (corresponding to mid-day in our core analysis region); and hourly surface albedo (Table S1 in Supporting Information). To capture the largest concentrations of aerosol in the ATAL, we focus mainly on mean distributions and profiles from MERRA-2 for July–September 2011–2020. Daily-mean data from May–September are used to illustrate the seasonal evolution of the MERRA-2 ATAL and its effects on clear-sky shortwave heating in the tropopause layer during 2011–2020, and daily means for July–September are used to assess variability. Regional selections are used to show variations in ATAL properties and radiative effects as functions of longitude (50°E–120°E, meridionally averaged over 22.5°N–25°N) and latitude (18°N–42°N, zonally averaged over 87.5°E–90°E) across the monsoon anticyclone. These two vertical cross-sections intersect at 22.5°N–25°N and 87.5°E–90°E, north of the Bay of Bengal. This 2.5°×2.5° grid cell is designated the 'core' region and is used to define the baseline for idealized radiative transfer calculations.

2.2 Radiative transfer model

Offline radiative transfer calculations to quantify ATAL effects on clear-sky shortwave radiative heating are conducted using version 2.0.3 of the libRadtran radiative transfer model (Mayer & Kylling, 2005; Emde et al., 2016), a multi-layer model developed to support flexible representation of absorption and scattering in the atmosphere. libRadtran is centered around the uvspec radiative transfer code, which can simulate radiative transfer across the solar and thermal spectra at a range of spectral resolutions (Mayer & Kylling, 2005; Emde et al., 2016). Default aerosol optical properties are from the Optical Properties of Aerosols and Clouds (OPAC) database (Hess et al., 1998), including radiative interactions of ten species of aerosols over wavelengths ranging from 250 nm to 40 µm across eight grades of relative humidity. OPAC also serves as the basis for aerosol optical properties in MERRA-2 (Chin et al., 2002; Randles et al., 2017; Buchard et al., 2017). Applications of libRadtran to shortwave radiative transfer and aerosol effects near the tropopause include development of remote sensing retrieval algorithms (Theys et al., 2007; Chen et al., 2020), assessments of the climate impacts of aviation (D. Lee et al., 2010; Schumann et al., 2021), evaluations of radiative transfer in chemistry–climate models (Forster et al., 2011), and cloud clearing for volcanic plumes (Kylling et al., 2015).

Our radiative transfer simulations use the DISORT (discrete ordinate) solver (Stamnes et al., 1988, 2000), which adopts a one-dimensional geometry under the plane parallel approximation to calculate radiative transfer across the solar spectrum. Reptran absorption parameterizations (Gasteiger et al., 2014) are used in the 'coarse' configuration, which corresponds to a spectral range of 240 nm–5 µm and a spectral resolution of 15 cm^{-1} (Emde et al., 2016), with approximately 5000 bands and 7500 wavelengths represented. Atmospheric background data include height, pressure, temperature, air density, ozone, oxy-

gen, water vapor, and CO_2. All data inputs are based on MERRA-2 model-level fields except for oxygen, which is taken from the libRadtran tropical default profile, and aerosol profiles from other products as indicated in section 4.2. Unless otherwise specified, solar zenith angle for radiative heating calculations is set to 0° for idealized simulations and the daily minimum at the corresponding latitude for geolocated simulations, while surface albedo is set to the local mean from MERRA-2 (0.15 for most calculations). These settings are both simple and helpful for emphasizing ATAL effects on radiative heating, which, as shown below, are largely insensitive to these two parameters. ATAL effects on TOA and surface fluxes are sensitive to these parameters, and are therefore computed in most scenarios by integrating over a representative diurnal cycle for Dhaka, Bangladesh.

Aerosol are specified according to OPAC as insoluble (INSO: hydrophobic organic carbon), water soluble (WASO: sulfate, nitrate, ammonium, hydrophilic black carbon, and hydrophilic organic carbon), or soot (SOOT: hydrophobic black carbon). To evaluate the impacts of including dust in the calculations, the accumulation and coarse modes of mineral dust (MIAM and MICM) are used according to the size bins simulated by MERRA-2. The benchmark profile for the control, or 'base', simulation is taken from mean conditions for July–September 2011–2020 within 22.5°N–25°N and 87.5°E–90°E, and excludes dust. Idealized simulations are then conducted to evaluate the impacts of changing the amplitude, composition, or peak height of the ATAL on clear-sky shortwave surface fluxes, TOA fluxes, and heating rates around the tropopause. We also evaluate changes in the solar zenith angle and surface albedo in an idealized setting and over typical diurnal and seasonal cycles. All idealized simulations, including the base case, only consider aerosol within the 60–180 hPa layer. This layer definition is based on many previous observations of ATAL aerosol loading, which place the ATAL between about 13–18 km (360–420 K potential temperature Vernier et al., 2011, 2017; Brunamonti et al., 2018; Hanumanthu et al., 2020; Zhang et al., 2020).

3 Aerosol layer description and idealized shortwave effects

3.1 ATAL distribution and composition in MERRA-2

Figure 1 shows distributions of sulfate, organic carbon, and black carbon within the UTLS (300 hPa–55 hPa) above the Asian monsoon region. Although dust accounts for the largest fraction by mass in the MERRA-2 UTLS (see also W. K. M. Lau et al., 2018), dust concentrations are weighted toward lower altitudes and the northern part of the anticyclone (Fig. S1 in Supporting information). The distribution of dust during July–September is consistent with dust transport from source regions in North Africa, the Middle East, and Central Asia in the subtropical westerly jet being entrained into the monsoon anticyclone and then lifted isentropically around the eastern flank of the anticyclone. Comparison with observational estimates (e.g., Vernier et al., 2017) and other datasets (Fig. S2 in Supporting Information) suggests that MERRA-2 overestimates dust concentrations at these levels. Moreover, our offline radiative transfer calculations (Fig. 5a) show that including dust at ATAL altitudes (60–180 hPa) has little impact on clear-sky shortwave heating rates. We therefore omit it from most of the following analysis.

ATAL aerosols are spread throughout the upper-level monsoon anticyclone at 100 hPa (Fig. 1a), with the largest concentrations along the southern flank near 370 K–375 K potential temperature (∼110 hPa; Fig. 1a–c). This distribution can be attributed to two key factors. First, the main convective sources of the ATAL as identified for MERRA-2 by W. K. M. Lau et al. (2018) are located upstream of the elongated maximum along the southern flank. Second, strong baroclinicity across the northern part of the anticyclone (the subtropical westerly jet) locates potential temperature surfaces at higher pressures (lower altitudes) in the north than in the south, while mean diabatic heating is positive but weak outside of deep convection (∼0.5 K day^{-1}; Tegtmeier et al., 2022, their Figs. 8.59-8.60). Transport within the anticyclone is mostly quasi-isentropic, with ascent

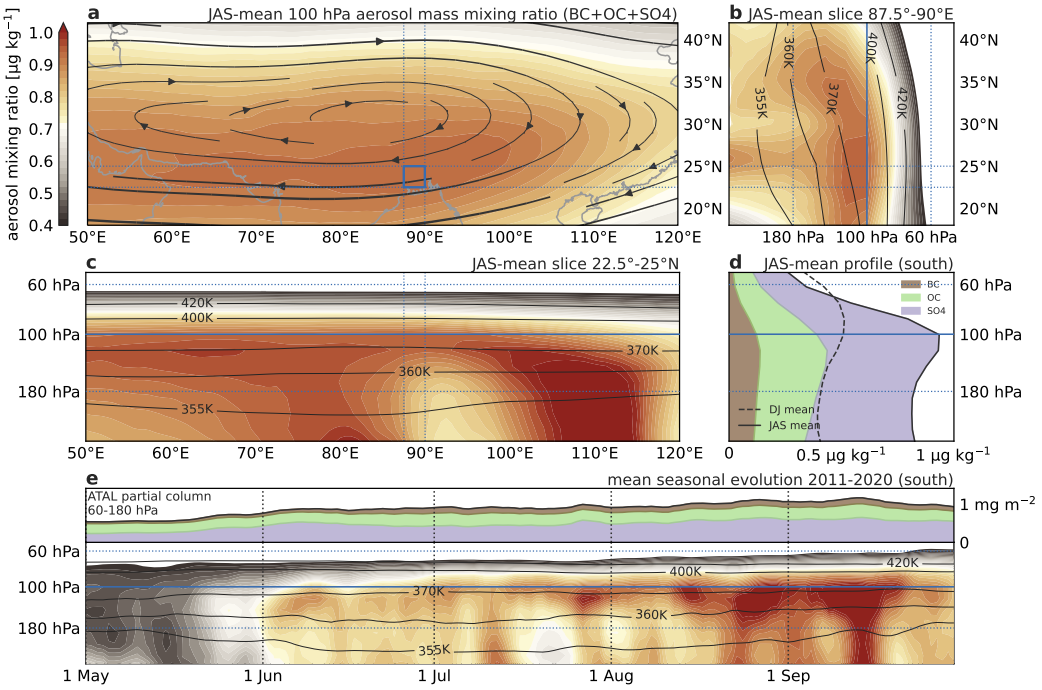

Figure 1. Distributions of sulfate, organic carbon, and black carbon aerosol mass mixing ratios based on the MERRA-2 aerosol reanalysis (a) as a function of latitude and longitude on the 100 hPa isobaric surface, (b) as a function of latitude and pressure along the 87.5°E–90°E longitude band, (c) as a function of longitude and pressure along the 22.5°N–25°N latitude band, and (d) as an area-average profile within 87.5°E–90°E and 22.5°N–25°N for July, August, and September 2011–2020. (e) Mean evolution of aerosol profile (lower panel) and partial column (vertically-integrated over 180–60 hPa; upper panel) within 87.5°E–90°E and 22.5°N–25°N from 1 May to 30 September 2011–2020. Streamlines in (a) show the upper-level anticyclone at 100 hPa based on MERRA-2. Contours in (b), (c), and (e) show potential temperature surfaces spanning the upper troposphere and lower stratosphere. Dashed line in (d) represents sum of sulfate, black carbon and organic carbon in December 2007 – January 2008. Shaded regions in (d) and (e) illustrate the relative abundances of black carbon (brown), organic carbon (green), and sulfate (purple) aerosol.

upward along isentropes in the east (where flow is north-to-south) and descent in the west (where flow is south-to-north). The isobaric aerosol distribution therefore shows larger values where the 370 K–375 K isentropic layer outcrops.

Cross-sections of mean ATAL vertical structure over July–September 2011–2020 are shown for the north-south (averaged zonally across 87.5°E–90°E; Fig. 1b) and east-west (averaged meridionally across 22.5°N–25°N) directions. The north-south cross-section cuts across the nominal center of the anticyclone above the eastern Tibetan Plateau, while the east-west cross-section slices eastward along the southern flank of the anticyclone (Fig. 1a). These cross-sections show a clearly defined ATAL peaking near the 370 K potential temperature surface (∼110 hPa along the east-west cross-section). This enhanced aerosol layer is fed by convective uplift between 20°N and 30°N with centers within 70°E–90°E (North India) and 105°E–115°E (Sichuan Basin and southern China; Fig. 1c). The aerosol maximum in the north-south cross-section largely follows isentropic contours (Fig. 1b) despite long transport distances around the anticyclone from the convective source regions. Enhanced aerosol loading in this altitude range develops mainly from the beginning of June and persists through the end of September, with the largest values in late August and early September.

Compared with W. K. M. Lau et al. (2018), our results suggest an additional 'chimney' over southern China (∼110°E; Fig. 1c), which is broader and shifted to the southeast relative to the Sichuan Basin source highlighted in their results. This peak could indicate persistent southeastward transport from the Sichuan Basin; however, the mean upper-level flow from the Sichuan Basin is southwestward (see also K.-O. Lee et al., 2021). We note further that W. K. M. Lau et al. (2018) analyzed only one monsoon season (May–August 2008) and did not include sulfate. There are thus several possible reasons for the difference between our results and theirs. First, it could be due to interannual variability in convective sources over East Asia (e.g., strong influences of convection over southern China during summer 2017; Bucci et al., 2020). Second, although local maxima in OC and BC are evident in that region (Figs. S3 and S4 in Supporting Information), they are much weaker than those over South Asia, and the chimney-like connection to the troposphere as in Fig. 1 appears only for sulfate (Fig. S5 in Supporting Information). Finally, the mean seasonal cycle in our core region, downstream of convection over southern China, suggests that sulfate loading in the ATAL is relatively small through most of July before increasing in August and peaking in early September (Fig. S5e in Supporting Information). This seasonality may reflect a strengthening convective source over southern China as the East Asian monsoon rainband retreats, changes in the efficiency of sulfate removal by deep convection over the Bay of Bengal (which starts early and peaks in July), or some combination of the two.

Within the MERRA-2 ATAL as defined in this work (60–180 hPa), sulfate is the largest component by mass fraction (43–61% for the ATAL column over the seasonal cycle; upper part of Fig. 1e). OC is next largest (28%–48%), with BC mass fractions smaller than OC by about a factor three (9%–16%). Notably, the hydrophilic component of OC is approximately in steady state through the monsoon development cycle (Fig. S4e), with the OC column almost completely hydrophilic in May and subsequent changes dominated by changes in the hydrophobic component. Here the ATAL column is obtained by integrating across the depth of the layer in pressure coordinates:

$$C_{\mathrm{ATAL}} = \frac{1}{g}\int_{p_b}^{p_t} q_{\mathrm{aer}} dp \tag{1}$$

where $g = 9.8\,\mathrm{m\,s^{-2}}$ is the gravitational acceleration, $p_b = 180\,\mathrm{hPa}$ is the base of the layer, $p_t = 60\,\mathrm{hPa}$ is the top of the layer, and q_{aer} is the aerosol mass mixing ratio. The OC and BC column masses calculated in this way are highly correlated ($r = 0.75$) but the majority of this is in the spatial dimension ($r = 0.88$), with much smaller covariability in time ($r = 0.59$). OC and sulfate are also highly correlated ($r = 0.64$), with

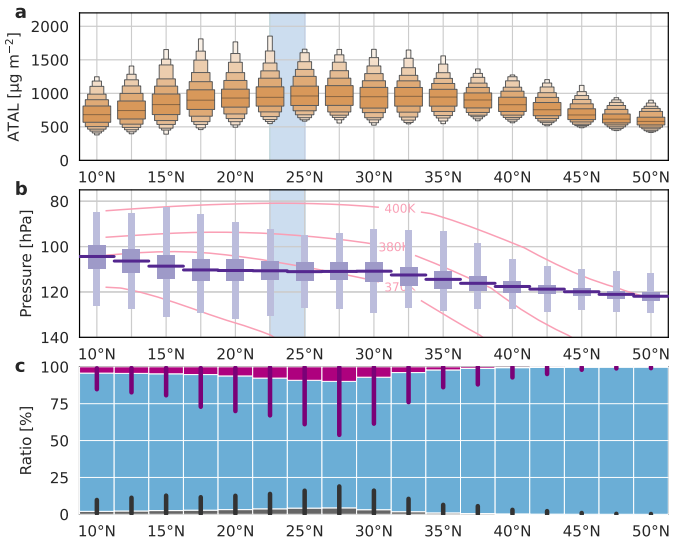

Figure 2. Variations in latitude of (a) distributions of daily-mean vertically-integrated aerosol mass per unit area in the 60–180 hPa layer; (b) box-and-whisker plots of ATAL height (in pressure) defined as the daily-mean center-of-mass (50% of ATAL mass both above and below); and (c) the soot (grey), water soluble (blue), and insoluble (purple) fractions of ATAL aerosol in 2.5° latitude bins along the 87.5°E–90°E longitude band. Minimum and maximum soot and insoluble fractions are indicated by thin grey and purple bars, respectively. Pink contours in (b) show potential temperature surfaces.

roughly equal correlations in space and time, while BC and sulfate are only weakly correlated ($r = 0.36$), especially in time ($r = 0.22$). Similar ranges of relative concentration are obtained for the mean vertical profile over July–September (Fig. 1d), with sulfate ratios ranging from 50% near the base of the layer at 180 hPa to 60% near the top of the layer at 60 hPa. OC mass fractions are consistently around 30% (28–33%) through the depth of the ATAL, while BC mass fractions decrease by half from the base of the layer (16%) to the top of the layer (8%). Given the weak temporal correlations and different vertical distributions of BC and sulfate within the ATAL, we treat these two species as nominally independent in setting up the idealized simulations below.

Figure 2 displays summary information about variations in selected ATAL properties by latitude along the same north-south cross-section as Fig. 1b. ATAL amplitude (Fig. 2a), calculated daily according to equation 1, peaks along the southern flank of the anticyclone around 20°N–25°N (Fig. 2a). The largest variations in daily-mean amplitude are located slightly south of the peak values (15°N–22.5°N) where, despite smaller median values, large outliers on the high end indicate episodes of strong convective uplift of polluted air. Variance reduces sharply with latitude northward of 35°N.

We estimate the daily height of the aerosol layer as its 'center of mass'. This is calculated by first integrating aerosol partial columns:

$$C(p) = \frac{1}{g} \int_{p}^{p_t} q_{\text{aer}} dp \tag{2}$$

for $p_b \leq p < p_t$, then calculating the ratio of $C(p)$ relative to C_{ATAL} (equation 1), and finally linearly interpolating the ratio in $\ln(p)$ to find the pressure associated with the ratio 0.5 (p_{com}). The results are not qualitatively sensitive to ratios between 0.25 and 0.75. Defined in this way, ATAL height decreases (p_{com} increases) from south to north,

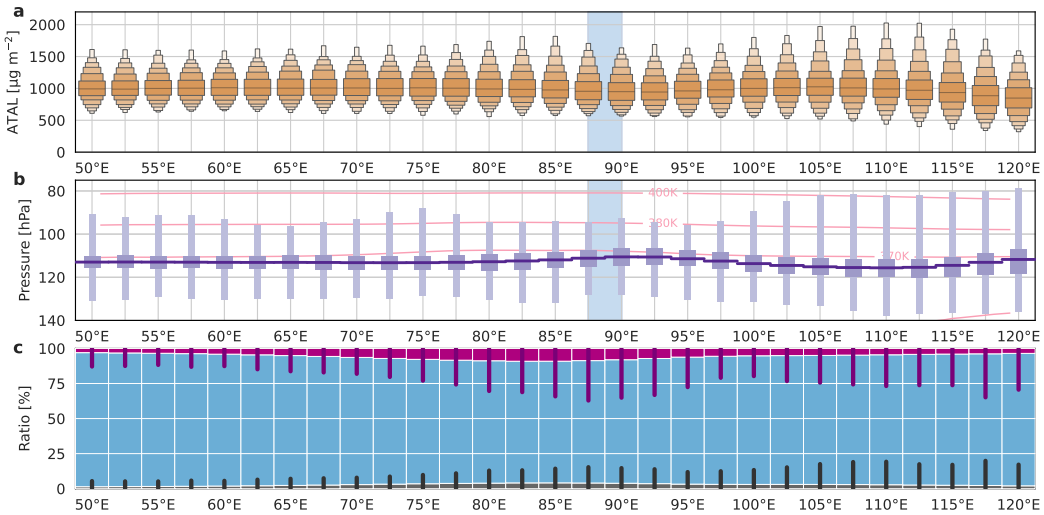

Figure 3. As in Fig. 2 but for variations in longitude within the 22.5°N–25°N latitude band.

with the largest variability at low latitudes. Daily-mean heights frequently lie above 370 K at all latitudes, with a few examples even reaching 400 K. ATAL heights are very consistent across the southern part of the anticyclone (20°N–30°N). Lower heights north of 30°N can be explained at least in part by the northward decline of isentropic surfaces toward higher pressures.

Relative composition of the mean ATAL layer is shown in Fig. 2c, here converted from the MERRA-2 species classification (sulfate, OC, BC) to the OPAC optical properties classification (WASO, INSO, SOOT). WASO is the largest fraction through the entire domain, consisting of sulfate and the hydrophilic components of OC and BC. SOOT (hydrophobic BC) and INSO (hydrophobic OC) fractions increase northward from low latitudes to 27.5°N, above the south slope of the Himalayas, and then decrease northward to the northern flank of the anticyclone around 40°N (the subtropical westerly jet). Distributions north of 40°N show little variability and are almost completely composed of sulfate. We therefore assume these distributions to be representative of extratropical stratospheric background aerosol and omit them from further analysis.

Average ATAL amplitude is fairly consistent as a function of longitude within the 22.5°N–25°N latitude band (Fig. 3a), although peaks in variance are evident around the two convective centers over North India (80°E–85°E) and southern China (105°E–115°E). Variance is especially large over the latter region, where the largest values of daily-mean C_{ATAL} exceed 2000 µg m^{-2}. Variations in ATAL height across longitudes (Fig. 3b) appear to be linked mainly to dilution and enhanced removal of the lower part of the layer by strong convection over the Bay of Bengal (near 90°E) and South China Sea (near 120°E). Composition fractions are consistent with the hypothesis that convection over North India (and the Sichuan Basin upstream) represent the main sources of carbonaceous aerosols, as the INSO and SOOT fractions are largest westward of 100°E. By contrast, the convective source over southern China has little impact on the relative concentrations of INSO and SOOT, consistent with this source providing mainly water soluble aerosols to the ATAL as represented in MERRA-2.

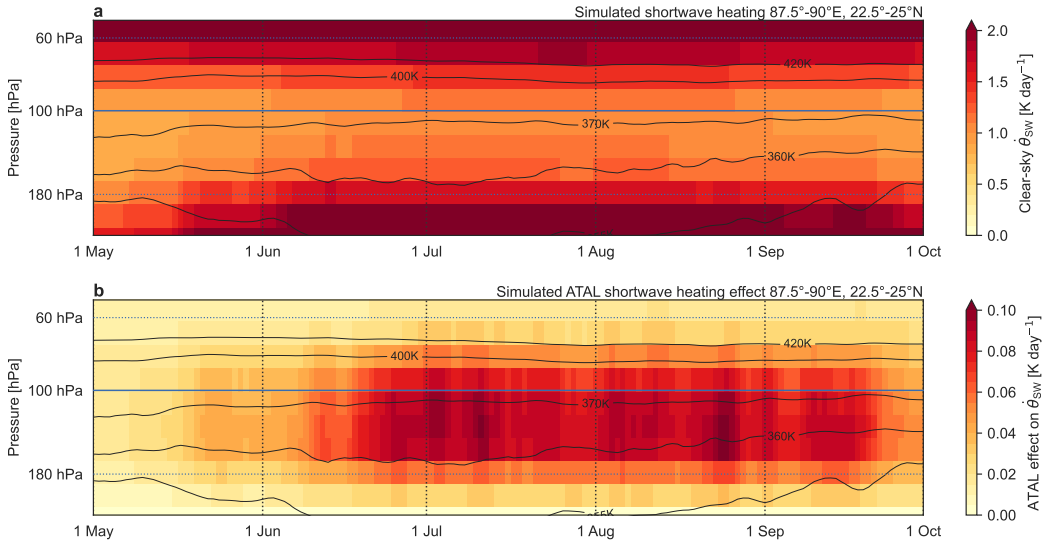

Figure 4. Mean seasonal evolution of (a) clear-sky shortwave heating and (b) the ATAL effect on clear-sky shortwave heating based on the MERRA-2 aerosol reanalysis. Radiative heating is calculated using offline radiative transfer simulations that account for seasonal changes in temperature, water vapor, ozone, ATAL aerosol (within 60–180 hPa), surface albedo, and the daily minimum solar zenith angle during 1 May–30 September 2011–2020. Heating rates have been divided by the Exner function to convert $\partial T/\partial t$ to $\dot{\theta}$ for ease of comparison to potential temperature contours.

3.2 Idealized simulations of ATAL effects on radiative heating

In this section, we summarize the results of offline radiative transfer calculations targeting different properties of the ATAL (Table 1). For context, Figure 4 shows the mean seasonal cycle of simulated shortwave heating for a clear-sky atmosphere with aerosol above the core region (22.5°N–25°N, 87.5°N–90°N), along with the aerosol contribution to this heating based on the evolution of ATAL aerosols shown in Fig. 1e. The ATAL radiative effect on clear-sky shortwave heating in this region grows slowly from mid-May before increasing sharply in mid-June (Fig. 4b). Aerosol effects on clear-sky shortwave heating persist at comparable levels until late September. These effects are strongest between 360 K and 400 K potential temperature, where clear-sky shortwave heating is at a minimum (Fig. 4a) Overall, the magnitude of the aerosol effect adds an additional heating of roughly 10% to clear-sky shortwave heating in the 100–150 hPa layer during the peak monsoon season. Evaluating ATAL effects relative to a wintertime aerosol profile rather than the no-aerosol profile reduces radiative heating effects by about half (Fig. S6).

Figure 5 shows aerosol effects on the surface flux, TOA flux, and radiative heating in the UTLS from the perspectives of ATAL amplitude, surface albedo, and solar zenith angle. The offline calculation for the base profile (i.e., adopting mean conditions for the core region) is compared to an offline calculation without aerosol and the online calculation from MERRA-2 in Figure 5a. The general structure of the profile is consistent with that from MERRA-2, but values are slightly smaller through most of the UTLS. These differences could result from nonlinearities in how the effects of shortwave absorbers scale; i.e., comparing an offline radiative calculation based on mean conditions (for which the cold point, hygropause, and ozone gradient are fixed in the vertical) to a mean of online profiles calculated from instantaneous conditions (for which the cold point, hygropause,

Table 1. Summary description of idealized radiative transfer calculations. All simulations use the same July–September (JAS) 2011–2020 mean atmospheric profile for 22.5°N–25°N and 87.5°E–90°E from MERRA-2. The base aerosol profile is similarly defined as JAS-mean BC+OC+SO_4 within 60–180 hPa. C_{ATAL} refers to aerosol column mass (eq. 1); $\mathrm{Prf}_{\mathrm{ATAL}}$ to the variation of aerosol type mass fractions with height; WASO, INSO, and SOOT to mass fractions of each aerosol type; SZA to solar zenith angle; and ALB to surface albedo.

Experiment	C_{ATAL}	$\mathrm{Prf}_{\mathrm{ATAL}}$	WASO	INSO	SOOT	SZA[a]	ALB[a]	Figure
amplitude	$n\times$base[b]	base	base	base	base	0°	0.15	Fig. 5b
solar	base	base	base	base	base	0–80°	0–0.25	Fig. 5c
diurnal	$n\times$base[b]	base	base	base	base	15 Aug[a]	15 Aug[a]	Fig. 6
composition	base	constant	0.6–1	0–0.4	0–0.2	0°	0.15	Fig. 7
height	selected[c]	base	selected	selected	selected	0°	0.15	Fig. 8
validation	product	product	product	product	product	0°	0.15	Fig. 12

[a] Solar parameters for TOA and surface fluxes specified as for Dhaka, Bangladesh on 15 August.
[b] n is a multiplier between 0.1 and 4.
[c] Daily mean profiles in each height bin are randomly selected from July–September 2011–2020.

and ozone gradient may vary in the vertical). They may also result from different assumptions about aerosol optical properties, as our conservative approach (assigning hydrophobic OC to INSO and hydrophilic OC and BC to WASO) minimizes the absorbing aerosol fraction. As ATAL effects scale linearly with amplitude and the relative composition of absorbing versus scattering aerosols (see below), we take the simulated aerosol effect from libRadtran as representative while accounting for these possible biases when computing relative effects.

Increasing the solar zenith angle from 0° to 40° has little impact on the ATAL effect on shortwave heating (Fig. 5c) owing to compensating effects between decreases in TOA insolation (proportional to the cosine of solar zenith angle) and increases in path length (inversely proportional to the cosine) as solar zenith angle increases. The heating effect weakens substantially as the solar zenith angle approaches 90°. Increasing surface albedo increases the ATAL effect on clear-sky shortwave heating, but these differences are small and require relatively large changes in the albedo. This sensitivity can be safely ignored for the clear-sky case in our core region as variations in surface albedo are small, but may be influential when the aerosol layer overlies thick anvil clouds or land ice, which are both present in abundance within the Asian monsoon domain. Changes in the no-aerosol radiative heating rates associated with changes in albedo and solar zenith angle are not shown, but are accounted for when computing the ATAL radiative effects.

Further context is provided by evaluating ATAL radiative effects across a representative diurnal cycle (Fig. 6). Integrated over the day, the upward flux at the nominal top-of-atmosphere (TOA) increases by about $0.04\,\mathrm{W\,m^{-2}}$, while the net downward (absorbed) flux of solar radiation at the surface decreases by about $0.32\,\mathrm{W\,m^{-2}}$ (Fig. 6a-b). The TOA radiative effect is about one third of that reported by Vernier et al. (2015), who estimated this effect to $0.12\,\mathrm{W\,m^{-2}}$. The difference between our estimate and theirs is further enhanced if we follow their approach and adopt a representative winter aerosol profile (dashed line in Fig. 1d) as the baseline in place of the no-aerosol case. With the same diurnal cycle of solar parameters, the decrease in surface absorption is reduced to $0.19\,\mathrm{W\,m^{-2}}$ while the change in the upward flux at TOA reverses sign to $-0.04\,\mathrm{W\,m^{-2}}$. The larger decrease in the surface effect relative to TOA implies a reduction in the ATAL heating, as seen also in Fig. S6 in comparison to Fig. 4. The difference in TOA effect in our calculations relative to that reported by Vernier et al. (2015) can be largely attributed

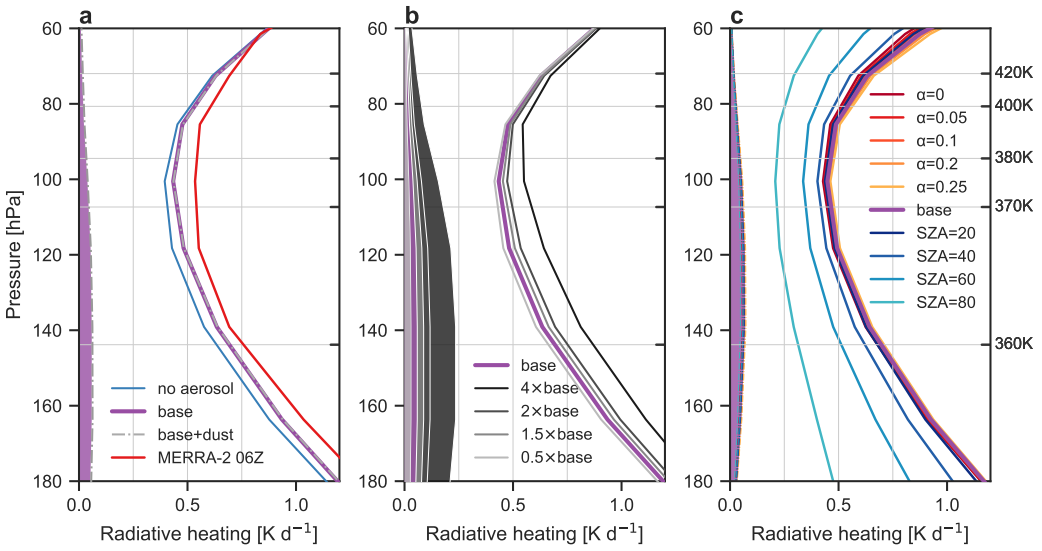

Figure 5. Radiative heating profiles calculated for (a) the no-aerosol (blue), base (purple; ATAL aerosol as in Fig. 1d within 60–180 hPa only), and base+dust (grey dash-dot line) profiles; (b) different ATAL amplitudes ranging from 0.5×base to 4×base without changing relative composition; and (c) for the base profile at selected values of solar zenith angle (SZA) and albedo (α); profiles in panels a and b are based on SZA = 0 and $\alpha = 0.15$. MERRA-2 clear-sky shortwave heating for local mid-day (04:30–07:30 UTC) is shown in c for comparison. Input data other than aerosols are specified as mean values for JAS 2011–2020 in 22.5°N–25°N and 87.5°E–90°E.

to the inclusion of BC (only OC and sulfate were considered in the calculations by Vernier et al., 2015), which enhances atmospheric absorption. We can retrieve a TOA effect of 0.12 W m^{-2} by raising the WASO fraction to 96% or higher (Fig. 7a), lowering the SOOT fraction to less than 2% (Fig. 7c), or increasing the base ATAL amplitude by a factor 3 (Fig. 6a). This last result underscores the linearity of the ATAL effect at both TOA and surface. Moreover, it highlights the relatively weak radiative impacts of dust within the ATAL. Including dust within the ATAL as represented by MERRA-2 for the core region increases the amplitude (i.e., the column mass per unit area) by a factor of 2.8, but only alters the TOA and surface effects by ∼10%, far less than scaling the base amplitude by a similar amount. As the additional decrease in surface absorption due to dust (∼0.03 W m^{-2}) is partially compensated by increased upward flux at TOA (∼0.01 W m^{-2}), its effect on radiative heating within the ATAL vertical range is very weak (Fig. 5a).

Diurnal variations in the ATAL effect on clear-sky shortwave heating are small over daylight hours (Fig. 6d). The largest sensitivities are found for the middle of the day, but effects are comparable in magnitude during the daytime except just after sunrise and just before sunset. Accordingly, given ∼13 hours of daylight, the mean ATAL effect on clear-sky shortwave heating integrated over 24 h is approximately half of that calculated for mid-day. To better emphasize the ATAL forcing on shortwave heating during daylight hours, we adopt a solar zenith angle of 0° for all further calculations and comparisons of radiative heating. By contrast, flux effects at TOA and surface are all integrated over 24 h to facilitate comparison with previous work.

We evaluate the effects of ATAL composition by holding the total concentration of anthropogenic aerosols fixed while changing the proportions of different species (Fig. 7). The ratios of all three species are vertically homogeneous in each experiment included

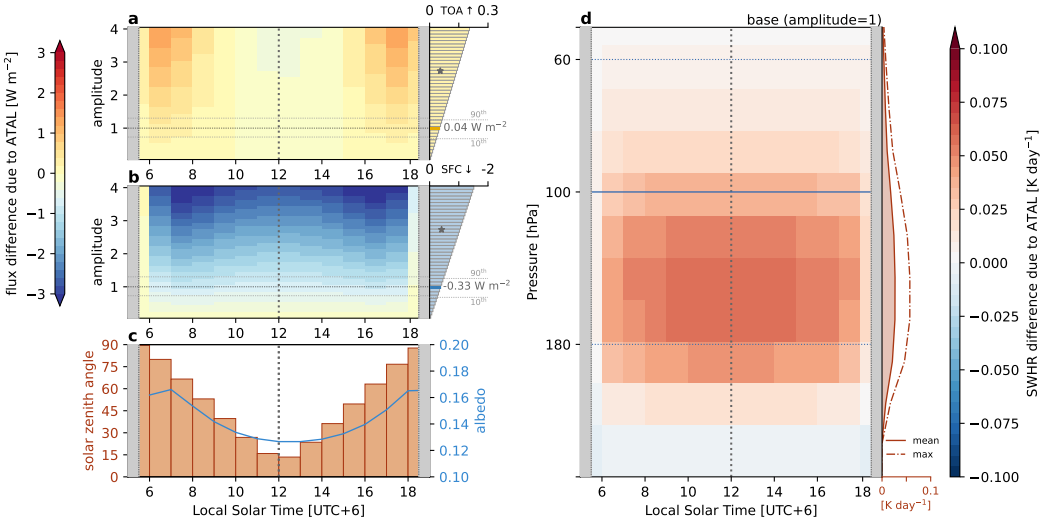

Figure 6. Diurnal variations of ATAL effects on clear-sky shortwave fluxes at (a) the top-of-atmosphere (TOA) and (b) clear-sky shortwave fluxes at the surface for ATAL amplitudes ranging from 0.1×base to 4×base; (c) diurnal variations in albedo (line) and solar zenith angle (bars), and (d) diurnal variations in ATAL effects on clear-sky shortwave heating for the ATAL base profile (aerosol within 60–180 hPa distributed as in Fig. 1d). All effects are calculated relative to no-aerosol simulations with matching solar parameters. Daily-mean values for ATAL effects on TOA flux, surface flux, and radiative heating are shown along the right margins of the corresponding panels, with values for the base profile highlighted. The 10$^{\text{th}}$ and 90$^{\text{th}}$ percentiles of ATAL column mass (eq. 1) for the core region in MERRA-2 are marked, as are the TOA and surface effects of including dust in addition to the base ATAL (grey stars).

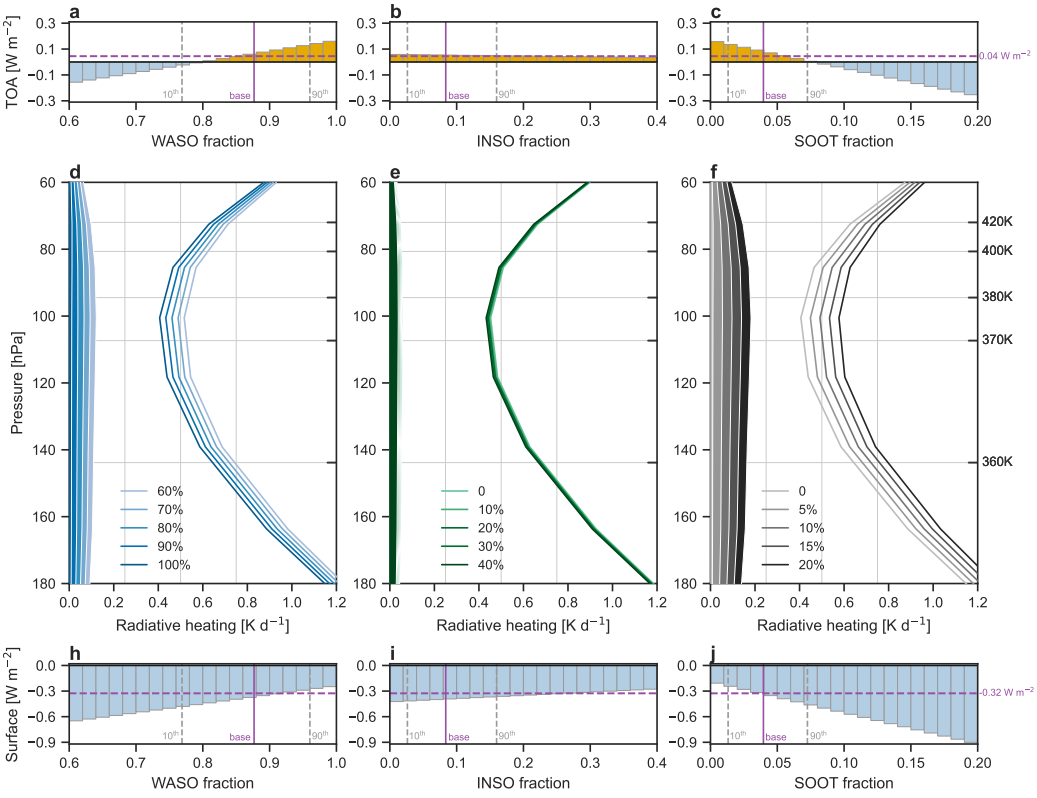

Figure 7. Variations in (a)–(c) top-of-atmosphere (TOA) shortwave flux anomalies, (d)–(f) vertical profiles of shortwave radiative heating in the tropopause layer, and (h)–(j) net surface shortwave flux anomalies under clear-sky conditions as a function of variations in the fractions of (a,d,h) water-soluble, (b,e,i) insoluble, and (c,f,j) soot relative to total aerosol. Mass fractions of each aerosol type are constant in height for each experiment. Heating rate profiles are calculated assuming a solar zenith angle of zero and a surface albedo of 0.15; TOA and surface fluxes are daily-mean values as in Fig. 6. Differences in heating relative to the no-aerosol case are shown as shaded regions on the left of panels d–f. The 10^{th} and 90^{th} percentiles of daily-mean ATAL column mass in the core region are marked as grey dashed vertical lines in panels 1–c and h–j, along with the base column mass (vertical purple line) and the TOA (a–c) or surface (h–j) flux effect calculated for base (dashed horizontal purple line).

in Fig. 7, resulting in different vertical structures relative to the base profile. Among the three OPAC aerosol types (WASO, INSO, SOOT), SOOT has the largest impact on radiative heating despite its small proportion (Fig. 7c). This large effect on clear-sky shortwave heating is consistent with its large capacity to absorb solar radiation (Samset et al., 2018). Compared to the other two types, SOOT has larger extinction coefficients across the solar spectrum and a consistently small single-scattering albedo, averaging ∼0.2 for wavelengths less than 1 µm (Hess et al., 1998). Extinction coefficients for WASO are approximately half of those for SOOT but with single-scattering albedos close to 1, while extinction coefficients for INSO are small by comparison (∼10% of those for WASO) with single-scattering albedos of approximately 0.8. The sensitivities in Fig. 7 may thus be understood as resulting largely from competition between a large fraction of scattering aerosols with moderate extinction coefficients and a small fraction of absorbing aerosols with large extinction coefficients. Increases in the former result in larger backscattering to the TOA (Fig. 7a), reduced ATAL heating near the tropopause (Fig. 7d), and a weaker reduction of net downward flux at the surface (Fig. 7h). Increases in the latter result in smaller backscattering (Fig. 7c), enhanced ATAL heating near the tropopause (Fig. 7f), and a stronger reduction of net downward flux at the surface (Fig. 7j). Although the INSO component is about twice as large as that for SOOT, small extinction coefficients mean that its impact in these scenarios is mainly to proportionately reduce both the absorbing and scattering effects while having little radiative impact itself. Note that brown carbon, as the absorbing component of OC (Samset et al., 2018), is not considered in these simulations, and hydrophilic BC is apportioned to WASO. Increasing the SOOT fraction as in Fig. 7f may thus be considered as a crude approximation to partitioning part of the hydrophobic OC to SOOT rather than INSO, or as retaining the hydrophilic fraction of BC in SOOT (Rémy et al., 2019).

Figure 8 shows results from sensitivity experiments evaluating the effects of varying the ATAL height. Here, height is defined as the 'center-of-mass' pressure level (p_{com}) for which 50% of the ATAL column by mass is located both between 60 hPa and p_{com} and between p_{com} and 180 hPa. For reference, p_{com} for the base profile is 112 hPa (Fig. 8c). Six height bins are defined, each with ten randomly selected daily-mean profiles for which p_{com} is within ±0.5 hPa of the specified level. Although total aerosol mass is the same in all simulations (Table 1), ATAL vertical structure (Fig. 8c) and composition (Fig. 8a-b) show substantial differences even within individual bins. These differences illustrate the scale of day-to-day variability in the ATAL as represented by MERRA-2. No clear dependence on ATAL height is evident in effects on either the TOA and surface fluxes or the tropopause-layer radiative heating. Instead, the results highlight the crucial influence of aerosol composition. Height bins for which a greater number of profiles have large SOOT mass fractions and small WASO mass fractions show a weaker enhancement of upward flux at the TOA, a stronger reduction in downward flux at the surface, and a larger influence on radiative heating near the tropopause. These relationships are replicated within each individual height bin (Fig. 8a-b).

The results shown in Fig. 8 exclude interdependence of height and amplitude by design. These two variables are significantly correlated in this region ($r = 0.62$) so that, on average, lower heights (larger p_{com}) are associated with a larger aerosol mass per unit area. We have previously shown that higher ATAL heights are mainly found where maritime deep convection may dilute or wash out the lower part of the aerosol layer (Fig. 1c; Fig. 3b). The relationships shown in Fig. 5b thus imply that aerosol effects on shortwave fluxes and heating rates are likely overestimated for height bins with $p_{\mathrm{com}} < 112$ hPa and underestimated for height bins with $p_{\mathrm{com}} > 112$ hPa in Fig. 8. Simulations based on varying the height of the peak aerosol concentration with composition fixed as in the base profile show a weak dependence on height (Fig. S7 in Supporting Information), with lower peaks associated with a weaker enhancement in upward flux at the TOA, a stronger reduction of downward shortwave flux, and an increase and downward shift of the maximum response in shortwave heating. However, these results also contain the influence

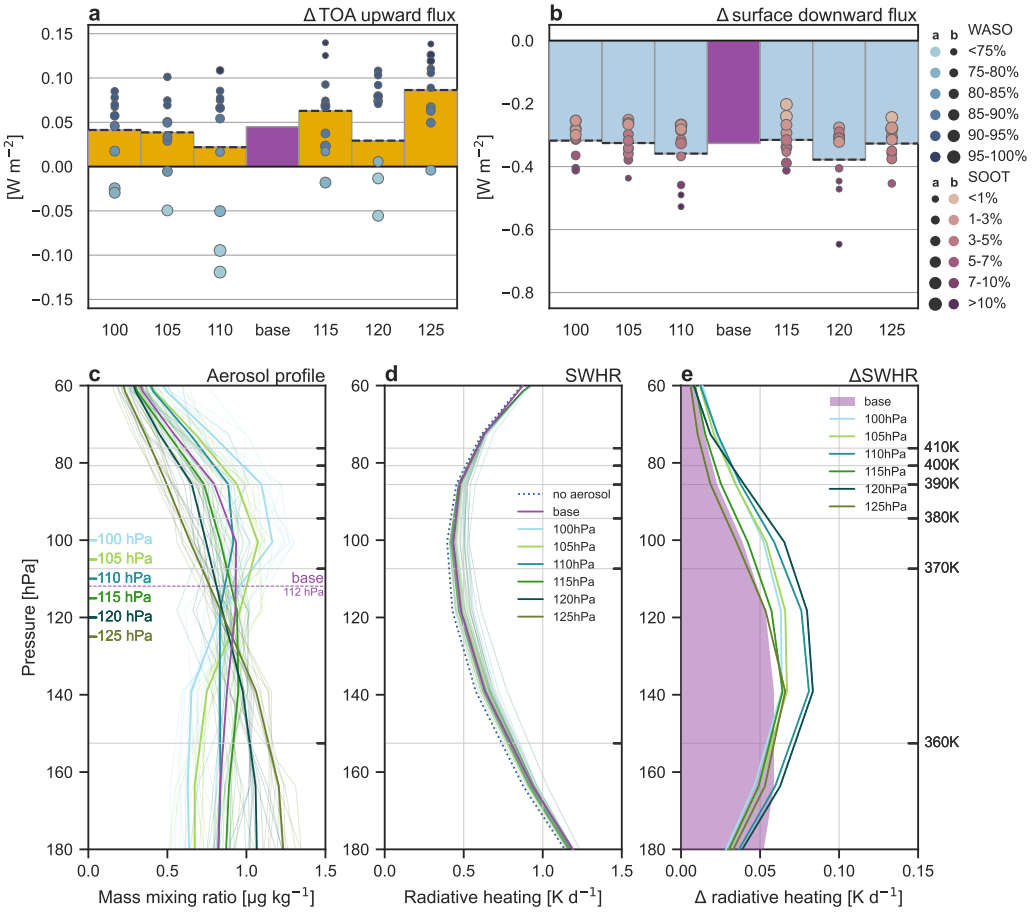

Figure 8. Variations in (a) top-of-atmosphere (TOA) upward shortwave flux anomalies, (b) surface downward shortwave net flux anomalies, (c) vertical profiles of aerosol mass mixing ratio, (d) shortwave radiative heating, and (e) aerosol effects on shortwave radiative heating relative to the no-aerosol case for profiles with different ATAL heights. Data for the 10 randomly selected daily-mean profiles from the core region (22.5°N–25°N, 87.5°E–90°E) are shown as round symbols in a-b (key at upper right) and light lines in c-d. Aerosol profiles are normalized to have the same column mass as the base profile in all experiments. Dashed black lines in a and b are included to confirm that mean results based on individual profiles agree well with results based on the mean profile. Heating rate profiles assume a solar zenith angle of zero and a surface albedo of 0.15; TOA and surface fluxes are daily-mean values as in Fig. 6.

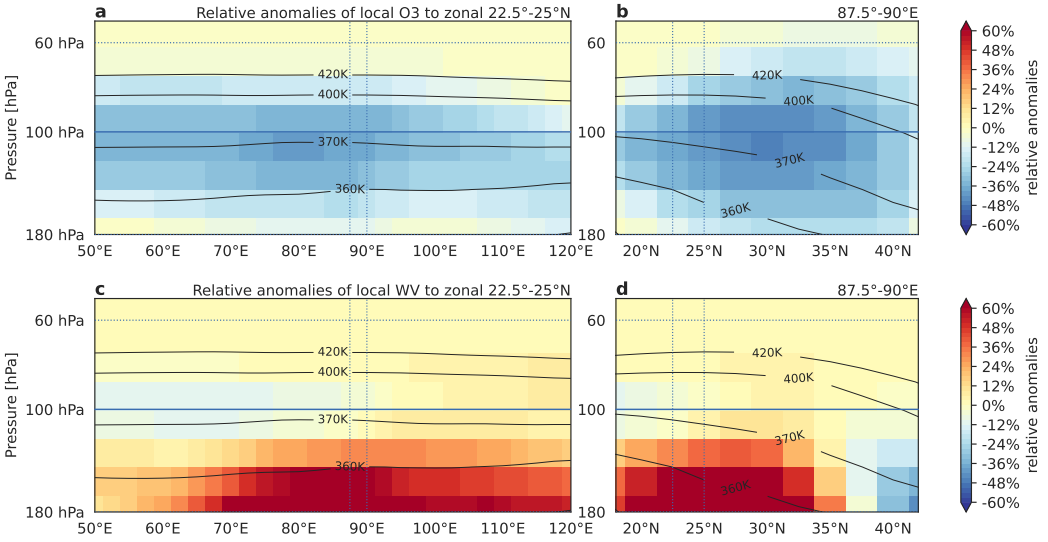

Figure 9. Anomalies in (a)–(b) ozone and (c)–(d) water vapor relative to the corresponding zonal mean profiles based on the MERRA-2 reanalysis for July–September 2011–2020. East–west cross-sections in (a) and (c) are averaged within the 22.5°N–25°N latitude band, while north–south cross-sections in (b) and (d) are averaged within the 87.5°E–90°E longitude band.

of changes in composition, as SOOT ratios are largest near the base of the layer while the top of the layer is almost entirely WASO.

4 Aerosol layer shortwave heating effects in context

4.1 Comparison to water vapor and ozone effects

To place the effects of the ATAL on radiative heating into context, we compare them to those of monsoon-driven perturbations in water vapor and ozone in the UTLS. When compared to the zonal mean, upper tropospheric humidity is substantially enhanced above the monsoon while ozone concentrations are relatively low (e.g., Santee et al., 2017), with the latter often referred to as an 'ozone valley' (e.g., Bian et al., 2020). Figure 9 shows anomalies in both ozone and water vapor relative to the zonal mean from MERRA-2 reanalysis products for July–September 2011–2020, again using the zonal and meridional cross-sections introduced in Fig. 1. Ozone concentrations are about 30% smaller than the zonal mean within the layer bounded by the 360 K and 420 K potential temperature surfaces. By contrast, water vapor is enhanced by approximately 30% relative to the zonal mean in the layer below ∼360 K, with a weak east–west dipole above. MERRA-2 relaxes model-generated water vapor concentrations to a zonal-mean climatology above 60 hPa, so that anomalies are constrained to remain close to zero in the lower stratosphere.

Figure 10 shows ATAL effects on radiative heating (Fig. 10a-b) in comparison to those of ozone (Fig. 10c-d) and water vapor (Fig. 10e-f).Aerosol effects are calculated relative to the no-aerosol case in each column, as in section 3.2 for the core region. Water vapor and ozone effects are calculated by replacing local mean mixing ratios of each component with zonal mean values at all levels between 60 hPa and 180 hPa. Radiative transfer calculations are then conducted for the original and perturbed profiles, with radiative effects defined as the difference (original minus perturbed).

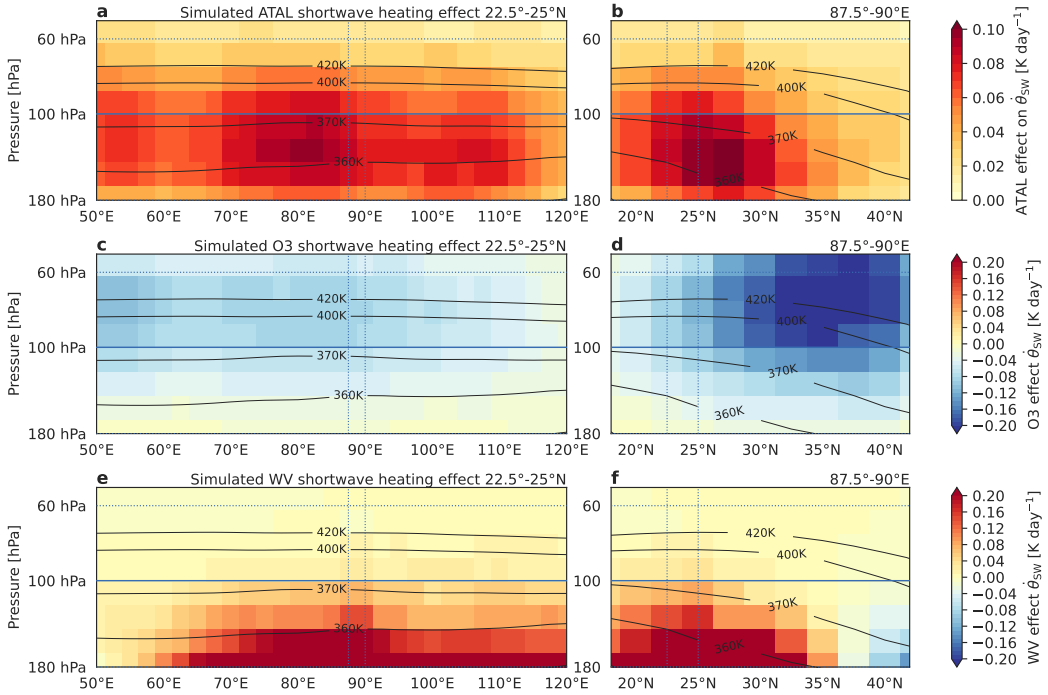

Figure 10. Effects on shortwave radiative heating attributed to (a)–(b) ATAL aerosol (60–180 hPa) relative to the no-aerosol simulation, (c)–(d) ozone anomalies relative to the zonal mean (see Fig. 9a–b) and (e)–(f) water vapor anomalies relative to the zonal mean (see Fig. 9c–d). Radiative effects in panels (a)–(f) are based on offline calculations under clear-sky conditions with surface albedo taken from MERRA-2 and solar zenith angle taken as the zonal minimum on 1 August. Heating rates have been divided by the Exner function to convert $\partial T/\partial t$ to $\dot{\theta}$ for ease of comparison to potential temperature contours.

Although maximum values of ozone and water vapor effects within the monsoon UTLS exceed that of the ATAL effect by about a factor two, values of the ATAL effect within the 360 K–420 K layer are comparable and often larger in magnitude, especially along the southern flank of the anticyclone (Fig. 10a-b). The ATAL effect is located at lower altitudes and is opposite in sign relative to the ozone effect (Fig. 10c-d). Water vapor effects are concentrated at lower altitudes, and are strongest along the southern flank of the anticyclone where convective sources are located (Fig. 10e-f). ATAL effects are of similar magnitude and often exceed the effects of the monsoon anomaly in water vapor within 370 K–420 K.

Overall, the ATAL influence on clear-sky shortwave heating can be thought of as a direct forcing that compensates for reduced shortwave absorption in the ozone valley while deepening and expanding the positive effects of water vapor. ATAL effects may be especially influential on diabatic heating in the western and northern parts of the anticyclone, where the positive effects of water vapor are weak but the negative impacts of the monsoon ozone valley are relatively strong. These are important regions for modifying the characteristics of air reaching the stratosphere. In stark contrast to the southeastern part of the anticyclone, temperatures in the west are relatively warm and relative humidities are relatively low owing to adiabatic compression while diabatic mass transport remains upward (Tegtmeier et al., 2022). Enhanced shortwave heating in these largely clear-sky regions of the anticyclone (see also Vernier et al., 2015) could poten-

tially help air to reach the stratosphere more quickly while avoiding the southeastern 'cold trap'; however, the net impact is not so simple to deduce. Additional diabatic heating can be partitioned in multiple ways. In one limit it can amplify local ascent, moving more air upward to smaller pressures without changing temperature. This possibility implies a weakening or reversal of local adiabatic warming and therefore increased humidity, with potential implications for concentrations of water vapor, short-lived halogenated species, and other components affected by the formation and sedimentation of ice. In the other limit it can result in local warming, shifting isentropic surfaces to larger pressures without changing pressure vertical velocities. Such a warming could enhance isentropic ascent around the anticyclone, but could also simply be balanced by enhanced longwave cooling via thermal relaxation either locally or downstream. These possibilities require evaluation in a comprehensive model framework that can represent coupled interactions between the ATAL and the anticyclone.

4.2 Discrepancies among aerosol reanalysis and forecast products

Several other recent reanalyses and forecasts of atmospheric composition are used to approximate uncertainty windows for ATAL effects on clear-sky shortwave radiative heating (Table 2). One of these, the Copernicus Atmosphere Monitoring Service (CAMS) and European Centre for Medium-range Weather Forecasts (ECMWF) Atmospheric Composition Reanalysis 4 (CAMS-EAC4; Inness et al., 2019) covers the entire period 2011–2020 but with a different model and data assimilation system and different emissions relative to MERRA-2 (Text S2 in Supporting Information). Three other products are used for July–September 2020 only. GEOS-FP is produced using a newer version of the same atmospheric model and data assimilation system as MERRA-2 (Lucchesi, 2018), but with a finer horizontal model grid and the inclusion of nitrate and ammonium aerosols. The CAMS atmospheric composition forecast product (CAMS-FC; Rémy et al., 2019) has a finer horizontal resolution and additional vertical levels relative to CAMS-EAC4, includes nitrate and ammonium aerosols where CAMS-EAC4 does not, and implements a more realistic coupling between sulfur dioxide and sulfate aerosols. Ten-day chemical forecasts based on the Whole Atmosphere Community Climate Model (WACCM; Gettelman et al., 2019) with interactive chemistry (Emmons et al., 2020) and aerosols (Liu et al., 2016) are also considered, with forecast initial conditions taken from GEOS-FP. Unlike MERRA-2, CAMS-EAC4, and GEOS-FP, AOD observations are not assimilated in the CAMS-FC or WACCM products used here.

These five products show significant differences in their representations of the ATAL above the monsoon core domain (22.5°N–25°N and 87.5°E–90°E; Fig. 11). GEOS-FP (Fig. 11c) and WACCM (Fig. 11f) each show ATAL amplitudes approximately twice as large as the other products, though with substantially different vertical distributions and compositions. In WACCM, OC is the largest contributor by mass in the lower part of the layer ($p > 100\,\mathrm{hPa}$), switching to sulfate in the upper part of the layer ($p < 100\,\mathrm{hPa}$). The maximum in aerosol mass mixing ratio is around 140–160 hPa. In GEOS-FP, concentrations of OC, nitrate, ammonium, and sulfate are all similar in magnitude throughout the depth of the ATAL, with each species (and total mass mixing ratio) peaking peaking much higher in the layer at ∼100 hPa. On the other side of the spectrum is the CAMS-EAC4 reanalysis (Fig. 11d), which produces a weak ATAL mostly composed of OC that peaks around 150 hPa. Results for CAMS-EAC4 from July–September 2020 are similar and are not shown here. OC in the CAMS-EAC4 ATAL is mainly hydrophobic in the lower part of the layer, while all other products indicate that hydrophilic OC outweighs hydrophobic OC through the full depth of the ATAL. The CAMS-FC product (Fig. 11e) includes nitrate and ammonium in addition to the species simulated in CAMS-EAC4. The OC fraction in CAMS-FC is again large in comparison to MERRA-2 and GEOS-FP, but unlike CAMS-EAC4 is primarily in the hydrophilic component. The distribution of sulfate is also considerably different, likely due to the revised coupling of SO_4 and SO_2 (Rémy et al., 2019). This change in the sulfate distribution relative to CAMS-EAC4

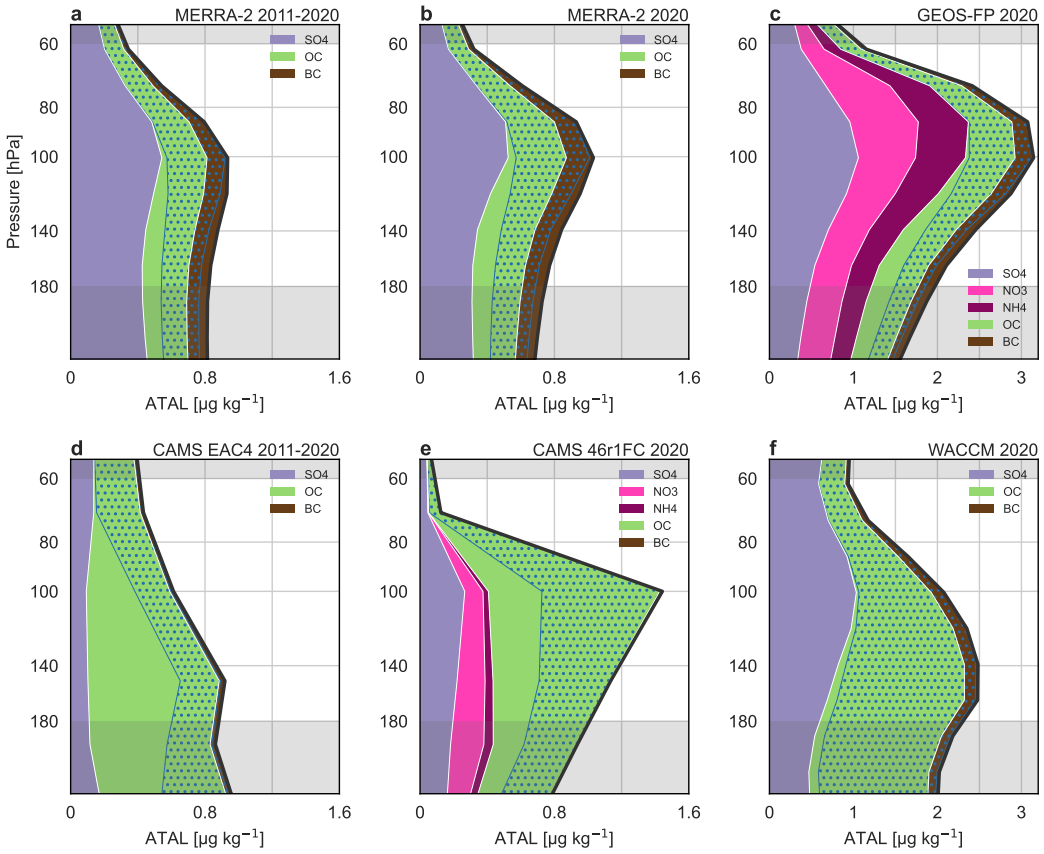

Figure 11. Comparison of ATAL vertical structure and composition in the core analysis region (22.5°N–25°N, 87.5°E–90°E) for (a) MERRA-2 during July–September (JAS) 2011–2020, (b) MERRA-2 during JAS 2020, (c) GEOS-FP during JAS 2020, (d) the CAMS reanalysis during JAS 2011–2020, (e) CAMS operational forecasts during JAS 2020, and (f) WACCM hindcasts during JAS 2020. The blue dotted regions mean hydroghilic organic carbon and hydrophilic black carbon. The range of the abscissa is expanded by a factor two in panels (c) and (f) relative to the other four. Among the five products shown, only the GEOS-FP and CAMS forecast products simulated nitrate and ammonium aerosol concentrations.

Table 2. Aerosol reanalysis and forecast products compared in section 4.2. ATAL effects on TOA and surface fluxes are included for reference.

Name	Years	Model	Aerosol species	ATAL effect
MERRA-2 (NASA)	2011–2020	GEOS 5.12.4 0.5°×0.625° 72 levels	BC, OC, dust SO_4	TOA: $0.04\,W\,m^{-2}$ SFC: $-0.33\,W\,m^{-2}$
GEOS-FP (NASA)	2020	GEOS 5.25.1 0.25°×0.3125° 72 levels	BC, OC, dust SO_4, NO_3, NH_4	TOA: $0.25\,W\,m^{-2}$ SFC: $-0.84\,W\,m^{-2}$
CAMS-EAC4 (ECMWF)	2011–2020	IFS Cy42r1 ∼80 km 60 levels	BC, OC, dust SO_4	TOA: $0.02\,W\,m^{-2}$ SFC: $-0.17\,W\,m^{-2}$
CAMS-FC (ECMWF)	2020	IFS Cy46r1 ∼40 km 137 levels	BC, OC, dust SO_4, NO_3, NH_4	TOA: $0.14\,W\,m^{-2}$ SFC: $-0.22\,W\,m^{-2}$
WACCM (NCAR)	2020	WACCM6 0.9°×1.25° 88 levels	BC, OC, dust SO_4, NH_4	TOA: $0.34\,W\,m^{-2}$ SFC: $-0.56\,W\,m^{-2}$

contributes to raising the peak mass mixing ratio to 100 hPa in CAMS-FC, but most of this increased ATAL height results from changes in OC. Both CAMS products indicate very small fractions of BC in the ATAL. BC loading in the middle and upper troposphere has been reported as overestimated in aerosol analyses that assimilate vertically-integrated AOD (Bozzo et al., 2020); however, it is not clear to what extent this applies to the ATAL, especially given substantial variations in the biomass burning source from year to year. A complementary presentation of differences in ATAL structure and composition is provided in Fig. S2 in Supporting Information.

Our intercomparison suggests that MERRA-2 may overestimate the mass fraction of BC within the ATAL but not necessarily the amount, as the latter is comparable to those simulated by GEOS-FP (with assimilation) and WACCM (without). However, the very small concentrations of BC in both CAMS-EAC4 and CAMS-FC are clearly incompatible with the relative abundance of BC in MERRA-2, GEOS-FP, and WACCM. Although explaining these differences exceeds the scope of this paper, our idealized experiments demonstrate significant implications for the magnitude of the ATAL effect on clear-sky shortwave heating (Fig. 7e). Comparing the ATAL from MERRA-2 to that from GEOS-FP suggests that omission of nitrate and ammonium may reduce the ATAL amplitude in MERRA-2 by about half, mainly impacting on the ratio of absorbing aerosol to scattering aerosol. If nitrate and ammonium are added to WASO, both differences are evaluated within the idealized radiative transfer calculations described in section 3.2. The qualitative distribution of sulfate is consistent across all products except for CAMS-EAC4, which shows little variation in height. Profiles of hydrophobic to hydrophilic ratios in OC and BC are also broadly consistent across all products except for CAMS-EAC4. The MERRA-2 ATAL is therefore not an outlier among these products, which supports our selection of this dataset as a baseline for the idealized calculations introduced above.

To clarify how uncertainties in ATAL structure and composition impact radiative heating near the tropopause, we replace the MERRA-2 ATAL in our base case with aerosol profiles from each product listed in Table 2. Other than aerosol loading in the 60–180 hPa layer, atmospheric conditions are identical for all simulations and no aerosols are included either above or below this layer. Figure 12 shows substantial differences in both the magnitude and the structure of ATAL effects on clear-sky shortwave heating, with the cor-

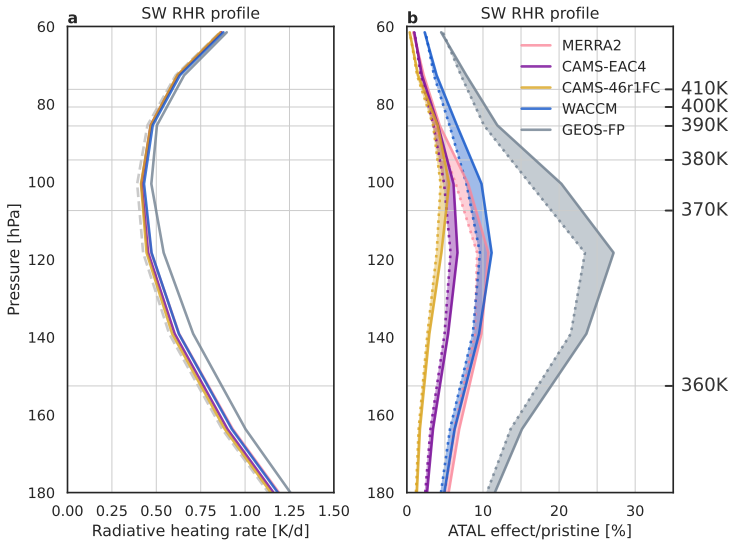

Figure 12. Vertical profiles of (a) clear-sky shortwave radiative heating within the tropopause layer calculated for the no-aerosol case (dashed grey line) and five ATAL profiles (60–180 hPa) from different products and (b) ATAL effects on clear-sky shortwave heating for the different aerosol products relative to the no-aerosol case both with (dotted) and without (solid) adjustment for smaller clear-sky heating rates in libRadtran relative to MERRA-2 (Fig. 5c). All aerosol profiles are time averages for July–September 2020 within the core analysis region (22.5°N–25°N, 87.5°E–90°E).

responding impacts on TOA and surface shortwave fluxes listed in Table 2. Consistent with smaller fractions of absorbing aerosols and weaker ATAL amplitudes, both CAMS-FC and CAMS-EAC4 produce radiative heating effects that are roughly half the size of those estimated for MERRA-2. Although the WACCM aerosol layer has approximately twice as much aerosol by mass as MERRA-2, a larger water soluble fraction and a smaller amount of hydrophobic black carbon result in similar effects on shortwave heating, with a smaller peak value but larger increases in heating in the upper part of the layer (Fig. 12b). The largest radiative effects throughout the layer are produced by GEOS-FP, which simulates larger fractions of absorbing aerosols in the lower part of the layer and larger concentrations of total aerosols in the upper part of the layer (Fig. S2). Aerosol effects on radiative heating are roughly twice as large when the MERRA-2 ATAL is replaced by that from GEOS-FP, corresponding to a 15–25% increase relative to clear-sky shortwave heating rates without aerosol. Accounting for smaller clear-sky shortwave heating based on libRadtran relative to MERRA-2 (Fig. 5a) reduces the amplitude of the simulated ATAL effect, but does not change its order of magnitude. Given conservative choices for optical properties (i.e., assigning the entirety of hydrophilic OC and BC to WASO and omitting any absorbing component of OC), it is unlikely that this difference leads us to overestimate the relative ATAL effect on shortwave heating as represented these five aerosol products. Indeed, interpreting part of the difference between the MERRA-2 and libRadtran profiles in Fig. 5a as a deficit in the aerosol contribution rather than the no-aerosol heating could increase the relative ATAL effect on clear-sky shortwave heating by a comparable or even larger amount.

5 Summary and outlook

This research has examined aerosol effects on shortwave fluxes at the surface and nominal top-of-atmosphere (TOA) along with radiative heating near the tropopause above the Asian monsoon. Our analysis confirms that MERRA-2 simulates a well-defined Asian tropopause aerosol layer composed of sulfate, carbonaceous aerosols, and dust (section 3.1). As emissions from volcanic eruptions are omitted after 2010 in MERRA-2 and dust is found to have little impact on radiative heating at these altitudes (Fig. 5a), the ATAL as examined above (sulfate plus carbonaceous aerosols) can be treated as mainly anthropogenic in origin. The ATAL is formed by Asian summer monsoon deep convection, with carbonaceous aerosols contributed mainly by deep convection over the Himalayan-Gangetic Plain and Sichuan Basin as previously reported by W. K. M. Lau et al. (2018) and a substantial convective source of sulfate over southern China (section 3.1). The latter is most influential during the late monsoon season (August–September).

Our simulations clarify ATAL impacts on clear-sky shortwave fluxes at the TOA and surface (section 3.2), with net effects for the time-mean ATAL relative to the no-aerosol case amounting to a $0.04\,\mathrm{W\,m^{-2}}$ reduction of incoming solar radiation at the TOA and a $0.32\,\mathrm{W\,m^{-2}}$ reduction in absorbed shortwave radiation at the surface. These effects increase linearly with increasing total ATAL mass per unit area while holding composition fixed or increasing (decreasing) relative mass fractions of scattering (absorbing) aerosol while holding total ATAL mass fixed. Comparison of these effects as simulated for recent aerosol analysis and forecast products (Table 2) shows large discrepancies in both, with the TOA effect varying by more than an order of magnitude and the surface effect varying by a factor 2–3. Aerosol effects on radiative heating account for around 10% of the clear-sky shortwave heating near the tropopause based on MERRA-2 (section 3.1), with a range of 5–25% calculated for other recent reanalysis and forecast aerosol products (section 4.2). Near the tropopause, ATAL effects based on MERRA-2 are comparable in magnitude to those of monsoon-related anomalies in ozone and water vapor (section 4.1), and are unique among these three in vertical location and horizontal extent. Possible implications for transport to the stratosphere are discussed at the end of section 4.1, but will require evaluation in model systems that represent coupled dynamical interactions between the ATAL and the monsoon anticyclone.

Although the inclusion of interactive aerosol within the meteorological reanalysis framework in MERRA-2 is undeniably helpful, there are large uncertainties that remain to be resolved. In particular, MERRA-2 and other analysis products that assimilate only vertically-integrated AOD may overestimate the abundance of absorbing aerosols at these altitudes (e.g., Bozzo et al., 2020). Assessment of this possibility is complicated by large regional and interannual variations in biomass burning sources and their proximity to convection. Moreover, nitrate aerosols, suggested to be a major component of the ATAL by observations (Höpfner et al., 2019) and some model simulations (Gu et al., 2016), are not represented in MERRA-2. Comparison with GEOS-FP, which uses a newer version of the same model, suggests that excluding nitrate may cause MERRA-2 to underestimate the amplitude of both the ATAL and its effects on radiative heating (section 4.2). However, the separability of absorbing and scattering aerosol contributions to ATAL radiative effects and the largely linear relationships to both components (section 3.2) offer promise for constraining the radiative and dynamical effects of these uncertainties, as they suggest that these effects could be represented within a relatively simple linearized framework. Future work will explore this possibility.

Open Research

MERRA-2 reanalysis products are available through the NASA Goddard Earth Sciences Data Information and Services Center (Global Modeling and Assimilation Office, 2015a, 2015b, 2015d, 2015c). The CAMS-EAC4 reanalysis (Copernicus Atmosphere Monitor-

ing Service, 2020) and CAMS forecast (Copernicus Atmosphere Monitoring Service, 2021) products are available through the Copernicus Atmosphere Data Store. WACCM forecast products are available through NCAR's Research Data Archive (dataset 313.6; Atmospheric Chemistry Observations & Modeling, National Center for Atmospheric Research, University Corporation for Atmospheric Research, 2020). The libRadtran radiative transfer model is available for download at http://www.libradtran.org.

Acknowledgments

This research has been supported by the Ministry of Science and Technology of the Peoples' Republic of China (project number 2017YFC1501404) and the National Natural Science Foundation of China (project number 41761134097). YH acknowledges a grant from the Natural Sciences and Engineering Research Council of Canada (RGPIN-2019-04511). The producers and providers of libRadtran and the various reanalysis and forecast products are gratefully acknowledged.

References

Albrecht, B. A. (1989). Aerosols, cloud microphysics, and fractional cloudiness. *Science*, *245*, 1227–1230. doi: 10.1126/science.245.4923.1227

Atmospheric Chemistry Observations & Modeling, National Center for Atmospheric Research, University Corporation for Atmospheric Research. (2020). *Whole Atmosphere Community Climate Model (WACCM) Model Output* [dataset]. Boulder, CO: Research Data Archive at the National Center for Atmospheric Research, Computational and Information Systems Laboratory. Retrieved from `https://rda.ucar.edu/datasets/ds313.6/`

Bergman, J. W., Fierli, F., Jensen, E. J., Honomichl, S., & Pan, L. L. (2013). Boundary layer sources for the Asian anticyclone: Regional contributions to a vertical conduit. *J. Geophys. Res. Atmos.*, *118*, 2560–2575. doi: 10.1002/jgrd.50142

Bian, J., Li, D., Bai, Z., Li, Q., Lyu, D., & Zhou, X. (2020). Transport of Asian surface pollutants to the global stratosphere from the Tibetan Plateau region during the Asian summer monsoon. *Natl. Sci. Rev.*, *7*, 516–533. doi: 10.1093/nsr/nwaa005

Bloom, S. C., Takacs, L. L., da Silva, A. M., & Ledvina, D. (1996). Data assimilation using incremental analysis updates. *Mon. Wea. Rev.*, *124*, 1256–1271. doi: 10.1175/1520-0493(1996)124⟨1256:DAUIAU⟩2.0.CO;2

Bossolasco, A., Jegou, F., Sellitto, P., Berthet, G., Kloss, C., & Legras, B. (2021). Global modeling studies of composition and decadal trends of the Asian Tropopause Aerosol Layer. *Atmos. Chem. Phys.*, *21*, 2745–2764. doi: 10.5194/acp-21-2745-2021

Bozzo, A., Benedetti, A., Flemming, J., Kipling, Z., & Rémy, S. (2020). An aerosol climatology for global models based on the tropospheric aerosol scheme in the Integrated Forecasting System of ECMWF. *Geosci. Model Dev.*, *13*(3), 1007–1034. doi: 10.5194/gmd-13-1007-2020

Brunamonti, S., Jorge, T., Oelsner, P., Hanumanthu, S., Singh, B. B., Kumar, K. R., ... Peter, T. (2018). Balloon-borne measurements of temperature, water vapor, ozone and aerosol backscatter on the southern slopes of the Himalayas during StratoClim 2016–2017. *Atmos. Chem. Phys.*, *18*, 15937–15957. doi: 10.5194/acp-18-15937-2018

Bucci, S., Legras, B., Sellitto, P., D'Amato, F., Viciani, S., Montori, A., ... Stroh, F. (2020). Deep-convective influence on the upper troposphere–lower stratosphere composition in the Asian monsoon anticyclone region: 2017 StratoClim campaign results. *Atmos. Chem. Phys.*, *20*(20), 12193–12210. doi: 10.5194/acp-20-12193-2020

Buchard, V., da Silva, A. M., Colarco, P. R., Darmenov, A., Randles, C. A., Govindaraju, R., ... Spurr, R. (2015). Using the OMI aerosol index and absorption aerosol optical depth to evaluate the NASA MERRA Aerosol Reanalysis. *Atmos. Chem. Phys.*, *15*(10), 5743–5760. doi: 10.5194/acp-15-5743-2015

Buchard, V., Randles, C. A., Silva, A. M. d., Darmenov, A., Colarco, P. R., Govindaraju, R., ... Yu, H. (2017). The MERRA-2 Aerosol Reanalysis, 1980 Onward. Part II: Evaluation and Case Studies. *J. Climate*, *30*(17), 6851–6872. doi: 10.1175/jcli-d-16-0613.1

Charlson, R. J., Schwartz, S. E., Hales, J. M., Cess, R. D., Coakley, J. A., Hansen, J. E., & Hofmann, D. J. (1992). Climate forcing by anthropogenic aerosols. *Science*, *255*, 423–430. doi: 10.1126/science.255.5043.423

Chen, Y., Chen, G., Cui, C., Zhang, A., Wan, R., Zhou, S., ... Fu, Y. (2020). Retrieval of the vertical evolution of the cloud effective radius from the Chinese FY-4 (Feng Yun 4) next-generation geostationary satellites. *Atmos. Chem. Phys.*, *20*(2), 1131–1145. doi: 10.5194/acp-20-1131-2020

Chin, M., Ginoux, P., Kinne, S., Torres, O., Holben, B. N., Duncan, B. N., ... Nakajima, T. (2002). Tropospheric aerosol optical thickness from the GOCART model and comparisons with satellite and sun photometer measurements. *J. Atmos. Sci.*, *59*, 461–483. doi: 10.1175/1520-0469(2002)059⟨0461:TAOTFT⟩2.0.CO;2

Colarco, P., Silva, A. d., Chin, M., & Diehl, T. (2010). Online simulations of global aerosol distributions in the NASA GEOS-4 model and comparisons to satellite and ground-based aerosol optical depth. *J. Geophys. Res. Atmos.*, *115*(D14), D14207. doi: 10.1029/2009jd012820

Colarco, P. R., Nowottnick, E. P., Randles, C. A., Yi, B., Yang, P., Kim, K.-M., ... Bardeen, C. G. (2014). Impact of radiatively interactive dust aerosols in the NASA GEOS-5 climate model: Sensitivity to dust particle shape and refractive index. *J. Geophys. Res. Atmos.*, *119*(2), 753–786. doi: 10.1002/2013jd020046

Copernicus Atmosphere Monitoring Service. (2020). *European Centre for Medium-range Weather Forecasts (ECMWF) Atmospheric Composition Reanalysis 4 (EAC4)* [dataset]. Reading, UK: Copernicus Atmosphere Data Store. Retrieved from `https://ads.atmosphere.copernicus.eu/cdsapp#!/dataset/cams-global-reanalysis-eac4-monthly`

Copernicus Atmosphere Monitoring Service. (2021). *CAMS Global Atmospheric Composition Forecasts* [dataset]. Reading, UK: Copernicus Atmosphere Data Store. Retrieved from `https://ads.atmosphere.copernicus.eu/cdsapp#!/dataset/cams-global-atmospheric-composition-forecasts`

Darmenov, A. S., & da Silva, A. M. (2015). *The quick fire emissions dataset (qfed): Documentation of versions 2.1, 2.2 and 2.4.* Technical Report Series on Global Modeling and Data Assimilation, No. 38, NASA/TM-2015-104606, Greenbelt, Maryland. (212 pp., available at https://ntrs.nasa.gov/citations/20180005253)

Diehl, T., Heil, A., Chin, M., Pan, X., Streets, D., Schultz, M., & Kinne, S. (2012). Anthropogenic, biomass burning, and volcanic emissions of black carbon, organic carbon, and SO_2 from 1980 to 2010 for hindcast model experiments. *Atmos. Chem. Phys. Discuss.*, *12*, 24895–24954. doi: 10.5194/acpd-12-24895-2012

Dong, B., Wilcox, L. J., Highwood, E. J., & Sutton, R. T. (2019). Impacts of recent decadal changes in Asian aerosols on the East Asian summer monsoon: roles of aerosol-radiation and aerosol-cloud interactions. *Clim. Dyn.*, *53*(5-6), 3235–3256. doi: 10.1007/s00382-019-04698-0

Emde, C., Buras-Schnell, R., Kylling, A., Mayer, B., Gasteiger, J., Hamann, U., ... Bugliaro, L. (2016). The libRadtran software package for radiative transfer calculations (version 2.0.1). *Geosci. Model Dev.*, *9*, 1647–1672. doi: 10.5194/gmd-9-1647-2016

Emmons, L. K., Schwantes, R. H., Orlando, J. J., Tyndall, G., Kinnison, D., Lamar-

que, J.-F., ... Pétron, G. (2020). The chemistry mechanism in the Community Earth System Model Version 2 (CESM2). *J. Adv. Model. Earth Syst.*, *12*(4), e2019MS001882. doi: 10.1029/2019MS001882

Fadnavis, S., Kalita, G., Kumar, K. R., Gasparini, B., & Li, J.-L. F. (2017). Potential impact of carbonaceous aerosol on the upper troposphere and lower stratosphere (UTLS) and precipitation during Asian summer monsoon in a global model simulation. *Atmos. Chem. Phys.*, *17*, 11637–11654. doi: 10.5194/acp-17-11637-2017

Fadnavis, S., Müller, R., Kalita, G., Rowlinson, M., Rap, A., Li, J.-L. F., ... Laakso, A. (2019). The impact of recent changes in Asian anthropogenic emissions of SO2 on sulfate loading in the upper troposphere and lower stratosphere and the associated radiative changes. *Atmos. Chem. Phys.*, *19*, 9989–10008. doi: 10.5194/acp-19-9989-2019

Flemming, J., Huijnen, V., Arteta, J., Bechtold, P., Beljaars, A., Blechschmidt, A.-M., ... Tsikerdekis, A. (2015). Tropospheric chemistry in the Integrated Forecasting System of ECMWF. *Geosci. Model Dev.*, *8*(4), 975–1003. Retrieved from `https://gmd.copernicus.org/articles/8/975/2015/` doi: 10.5194/gmd-8-975-2015

Forster, P. M., Fomichev, V. I., Rozanov, E., Cagnazzo, C., Jonsson, A. I., Langematz, U., ... Shibata, K. (2011). Evaluation of radiation scheme performance within chemistry climate models. *J. Geophys. Res. Atmos.*, *116*(D10), D10302. doi: 10.1029/2010JD015361

Fu, R., Hu, Y., Wright, J. S., Jiang, J. H., Dickinson, R. E., Chen, M., ... Wu, D. L. (2006). Short circuit of water vapor and polluted air to the global stratosphere by convective transport over the tibetan plateau. *Proc. Natl. Acad. Sci. U.S.A.*, *103*, 5664–5669. doi: 10.1073/pnas.0601584103

Garny, H., & Randel, W. J. (2013). Dynamic variability of the Asian monsoon anticyclone observed in potential vorticity and correlations with tracer distributions. *J. Geophys. Res. Atmos.*, *118*(24), 13,421-13,433. doi: 10.1002/2013JD020908

Gasteiger, J., Emde, C., Mayer, B., Buras, R., Buehler, S., & Lemke, O. (2014). Representative wavelengths absorption parameterization applied to satellite channels and spectral bands. *J. Quant. Spectrosc. Radiat. Transfer*, *148*, 99–115. doi: 10.1016/j.jqsrt.2014.06.024

Gelaro, R., McCarty, W., Suárez, M. J., Todling, R., Molod, A., Takacs, L., ... Zhao, B. (2017). The Modern-Era Retrospective Analysis for Research and Applications, Version 2 (MERRA-2). *J. Climate*, *30*(14), 5419–5454. doi: 10.1175/JCLI-D-16-0758.1

Gettelman, A., Mills, M. J., Kinnison, D. E., Garcia, R. R., Smith, A. K., Marsh, D. R., ... Randel, W. J. (2019). The Whole Atmosphere Community Climate Model Version 6 (WACCM6). *J. Geophys. Res. Atmos.*, *124*(23), 12380–12403. doi: 10.1029/2019JD030943

Global Modeling and Assimilation Office. (2015a). *MERRA-2 inst3_3d_aer_Nv: 3d, 3-Hourly, Instantaneous, Model-Level, ssimilation, Aerosol Mixing Ratio V5.12.4* [dataset]. NASA Goddard Earth Sciences Data and Information Services Center. doi: 10.5067/LTVB4GPCOTK2

Global Modeling and Assimilation Office. (2015b). *MERRA-2 inst3_3d_asm_Nv: 3d, 3-Hourly, Instantaneous, Model-Level, Assimilation, Assimilated Meteorological Fields V5.12.4* [dataset]. NASA Goddard Earth Sciences Data and Information Services Center. doi: 10.5067/WWQSXQ8IVFW8

Global Modeling and Assimilation Office. (2015c). *MERRA-2 tavg1_2d_rad_Nx: 2d, 1-Hourly, Time-Averaged, Single-Level, Assimilation, Radiation Diagnostics V5.12.4* [dataset]. NASA Goddard Earth Sciences Data and Information Services Center. doi: 10.5067/Q9QMY5PBNV1T

Global Modeling and Assimilation Office. (2015d). *MERRA-2 tavg3_3d_rad_Nv:*

3d, 3-Hourly, Time-Averaged, Model-Level, Assimilation, Radiation Diagnostics V5.12.4 [dataset]. NASA Goddard Earth Sciences Data and Information Services Center. doi: 10.5067/7GFQKO1T43RW

Granier, C., Bessagnet, B., Bond, T., D'Angiola, A., Gon, H. D. v. d., Frost, G. J., ... Vuuren, D. P. v. (2011). Evolution of anthropogenic and biomass burning emissions of air pollutants at global and regional scales during the 1980–2010 period. *Clim. Change*, *109*(1-2), 163. doi: 10.1007/s10584-011-0154-1

Gu, Y., Liao, H., & Bian, J. (2016). Summertime nitrate aerosol in the upper troposphere and lower stratosphere over the Tibetan Plateau and the South Asian summer monsoon region. *Atmos. Chem. Phys.*, *16*(11), 6641–6663. doi: 10.5194/acp-16-6641-2016

Guenther, A., Hewitt, C. N., Erickson, D., Fall, R., Geron, C., Graedel, T., ... Zimmerman, P. (1995). A global model of natural volatile organic compound emissions. *J. Geophys. Res. Atmos.*, *100*(D5), 8873–8892. doi: 10.1029/94JD02950

Hanumanthu, S., Vogel, B., Müller, R., Brunamonti, S., Fadnavis, S., Li, D., ... Peter, T. (2020). Strong day-to-day variability of the Asian Tropopause Aerosol Layer (ATAL) in August 2016 at the Himalayan foothills. *Atmos. Chem. Phys.*, *20*(22), 14273–14302. doi: 10.5194/acp-20-14273-2020

He, Q., Ma, J., Zheng, X., Wang, Y., Wang, Y., Mu, H., ... Lelieveld, J. (2021). Formation and dissipation dynamics of the Asian tropopause aerosol layer. *Environ. Res. Lett.*, *16*(1), 014015. doi: 10.1088/1748-9326/abcd5d

Hess, M., Koepke, P., & Schult, I. (1998). Optical Properties of Aerosols and Clouds: The software package OPAC. *Bull. Am. Meteor. Soc.*, *79*, 831–844. doi: 10.1175/1520-0477(1998)079⟨0831:opoaac⟩2.0.co;2

Höpfner, M., Ungermann, J., Borrmann, S., Wagner, R., Spang, R., Riese, M., ... Wohltmann, I. (2019). Ammonium nitrate particles formed in upper troposphere from ground ammonia sources during Asian monsoons. *Nature Geosci.*, *12*, 608–612. doi: 10.1038/s41561-019-0385-8

Hoskins, B. J., & Rodwell, M. J. (1995). A model of the Asian summer monsoon. Part I: the global scale. *J. Atmos. Sci.*, *52*, 1329–1340. doi: 10.1175/1520-0469(1995)052⟨1329:amotas⟩2.0.co;2

Inness, A., Ades, M., Agustí-Panareda, A., Barré, J., Benedictow, A., Blechschmidt, A.-M., ... Suttie, M. (2019). The CAMS reanalysis of atmospheric composition. *Atmos. Chem. Phys.*, *19*(6), 3515–3556. doi: 10.5194/acp-19-3515-2019

Janssens-Maenhout, G. (2010). *EDGARv4.1 Emission Maps* [dataset]. European Commission, Joint Research Centre (JRC). (http://data.europa.eu/89h/jrc-edgar-emissionmapsv41)

Janssens-Maenhout, G. (2011). *EDGARv4.2 Emission Maps* [dataset]. European Commission, Joint Research Centre (JRC). (http://data.europa.eu/89h/jrc-edgar-emissionmapsv42)

Kaiser, J. W., Heil, A., Andreae, M. O., Benedetti, A., Chubarova, N., Jones, L., ... van der Werf, G. R. (2012). Biomass burning emissions estimated with a global fire assimilation system based on observed fire radiative power. *Biogeosciences*, *9*(1), 527–554. doi: 10.5194/bg-9-527-2012

Kinne, S., Schulz, M., Textor, C., Guibert, S., Balkanski, Y., Bauer, S. E., ... Tie, X. (2006). An AeroCom initial assessment – optical properties in aerosol component modules of global models. *Atmos. Chem. Phys.*, *6*, 1815–1834. doi: 10.5194/acp-6-1815-2006

Kreidenweis, S. M., Petters, M., & Lohmann, U. (2019). 100 years of progress in cloud physics, aerosols, and aerosol chemistry. *Meteorol. Monogr.*, *59*, 11.1–11.72. doi: 10.1175/amsmonographs-d-18-0024.1

Kuniyal, J. C., & Guleria, R. P. (2018). The current state of aerosol-radiation interactions: A mini review. *J. Aerosol Sci.*, *130*, 45–54. doi: 10.1016/j.jaerosci.2018.12.010

Kylling, A., Kristiansen, N., Stohl, A., Buras-Schnell, R., Emde, C., & Gasteiger, J. (2015). A model sensitivity study of the impact of clouds on satellite detection and retrieval of volcanic ash. *Atmos. Meas. Tech.*, *8*(5), 1935–1949. doi: 10.5194/amt-8-1935-2015

Lau, K.-M., & Kim, K.-M. (2006). Observational relationships between aerosol and Asian monsoon rainfall, and circulation. *Geophysical Research Letters*, *33*, L21810. doi: 10.1029/2006GL027546

Lau, W. K. M., Yuan, C., & Li, Z. (2018). Origin, maintenance and variability of the Asian Tropopause Aerosol Layer (ATAL): The roles of monsoon dynamics. *Scientific Reports*, *8*, 3960. doi: 10.1038/s41598-018-22267-z

Lee, D., Pitari, G., Grewe, V., Gierens, K., Penner, J., Petzold, A., ... Sausen, R. (2010). Transport impacts on atmosphere and climate: Aviation. *Atmos. Environ.*, *44*(37), 4678–4734. (Transport Impacts on Atmosphere and Climate: The ATTICA Assessment Report) doi: 10.1016/j.atmosenv.2009.06.005

Lee, K.-O., Barret, B., Flochmoën, E. L., Tulet, P., Bucci, S., Hobe, M. v., ... Ulanovsky, A. (2021). Convective uplift of pollution from the Sichuan Basin into the Asian monsoon anticyclone during the StratoClim aircraft campaign. *Atmos. Chem. Phys.*, *21*(5), 3255–3274. doi: 10.5194/acp-21-3255-2021

Legras, B., & Bucci, S. (2020). Confinement of air in the Asian monsoon anticyclone and pathways of convective air to the stratosphere during the summer season. *Atmos. Chem. Phys.*, *20*(18), 11045–11064. doi: 10.5194/acp-20-11045-2020

Lelieveld, J., Bourtsoukidis, E., Brühl, C., Fischer, H., Fuchs, H., Harder, H., ... Ziereis, H. (2018). The South Asian monsoon–Pollution pump and purifier. *Science*, *361*(6399), eaar2501. doi: 10.1126/science.aar2501

Liu, X., Ma, P.-L., Wang, H., Tilmes, S., Singh, B., Easter, R. C., ... Rasch, P. J. (2016). Description and evaluation of a new four-mode version of the Modal Aerosol Module (MAM4) within version 5.3 of the Community Atmosphere Model. *Geosci. Model Dev.*, *9*(2), 505–522. doi: 10.5194/gmd-9-505-2016

Lohmann, U. (2017). Anthropogenic aerosol influences on mixed-phase clouds. *Curr. Clim. Change Rep.*, *3*(1), 32–44. doi: 10.1007/s40641-017-0059-9

Lucchesi, R. (2018). *File specification for GEOS-5 FP.* GMAO Office Note No. 4 (version 1.2), Greenbelt, Maryland. (62 pp., available at http://gmao.gsfc.nasa.gov/pubs/office_notes)

Ma, J., Brühl, C., He, Q., Steil, B., Karydis, V. A., Klingmüller, K., ... Lelieveld, J. (2019). Modeling the aerosol chemical composition of the tropopause over the Tibetan Plateau during the Asian summer monsoon. *Atmos. Chem. Phys.*, *19*(17), 11587–11612. doi: 10.5194/acp-19-11587-2019

Mahnke, C., Weigel, R., Cairo, F., Vernier, J.-P., Afchine, A., Krämer, M., ... Borrmann, S. (2021). The Asian tropopause aerosol layer within the 2017 monsoon anticyclone: microphysical properties derived from aircraft-borne in situ measurements. *Atmos. Chem. Phys.*, *21*(19), 15259–15282. doi: 10.5194/acp-21-15259-2021

Mayer, B., & Kylling, A. (2005). Technical note: The libRadtran software package for radiative transfer calculations - description and examples of use. *Atmos. Chem. Phys.*, *5*, 1855–1877. doi: 10.5194/acp-5-1855-2005

Neely, R. R., Yu, P., Rosenlof, K. H., Toon, O. B., Daniel, J. S., Solomon, S., & Miller, H. L. (2014). The contribution of anthropogenic SO2 emissions to the Asian tropopause aerosol layer. *J. Geophys. Res. Atmos.*, *119*, 1571–1579. doi: 10.1002/2013jd020578

Neely III, R., & Schmidt, A. (2016). *Volcaneesm: Global volcanic sulphur dioxide (so2) emissions database from 1850 to present - version 1.0* [dataset]. NERC Centre for Environmental Data Analysis (CEDA). Retrieved from `https://catalogue.ceda.ac.uk/uuid/a8a7e52b299a46c9b09d8e56b283d385` doi: 10.5285/76EBDC0B-0EED-4F70-B89E-55E606BCD568

Orbe, C., Waugh, D. W., & Newman, P. A. (2015). Air-mass origin in the tropical

lower stratosphere: The influence of Asian boundary layer air. *Geophys. Res. Lett.*, *42*(10), 4240–4248. doi: 10.1002/2015gl063937

Pan, L. L., Honomichl, S. B., Kinnison, D. E., Abalos, M., Randel, W. J., Bergman, J. W., & Bian, J. (2016). Transport of chemical tracers from the boundary layer to stratosphere associated with the dynamics of the Asian summer monsoon. *J. Geophys. Res. Atmos.*, *121*, 14159–14174. doi: 10.1002/2016jd025616

Park, M., Randel, W. J., Gettelman, A., Massie, S. T., & Jiang, J. H. (2007). Transport above the Asian summer monsoon anticyclone inferred from Aura Microwave Limb Sounder tracers. *J. Geophys. Res. Atmos.*, *112*, D16309. doi: 10.1029/2006jd008294

Ploeger, F., Konopka, P., Walker, K., & Riese, M. (2017). Quantifying pollution transport from the Asian monsoon anticyclone into the lower stratosphere. *Atmos. Chem. Phys.*, *17*, 7055–7066. doi: 10.5194/acp-17-7055-2017

Ramaswamy, V., Collins, W., Haywood, J., Lean, J., Mahowald, N., Myhre, G., ... Storelvmo, T. (2018). Radiative forcing of climate: The historical evolution of the radiative forcing concept, the forcing agents and their quantification, and applications. *Meteorol. Monogr.*, *59*, 14.1 - 14.101. doi: 10.1175/AMSMONOGRAPHS-D-19-0001.1

Randel, W. J., Park, M., Emmons, L., Kinnison, D., Bernath, P., Walker, K. A., ... Pumphrey, H. (2010). Asian monsoon transport of pollution to the stratosphere. *Science*, *328*, 611–613. doi: 10.1126/science.1182274

Randerson, J. T., Liu, H., Flanner, M. G., Chambers, S. D., Jin, Y., Hess, P. G., ... Zender, C. S. (2006). The impact of boreal forest fire on climate warming. *Science*, *314*(5802), 1130–1132. doi: 10.1126/science.1132075

Randles, C. A., Silva, A. M. d., Buchard, V., Colarco, P. R., Darmenov, A., Govindaraju, R., ... Flynn, C. J. (2017). The MERRA-2 Aerosol Reanalysis, 1980 onward. Part I: System description and data assimilation evaluation. *J. Climate*, *30*, 6823–6850. doi: 10.1175/jcli-d-16-0609.1

Rémy, S., Kipling, Z., Flemming, J., Boucher, O., Nabat, P., Michou, M., ... Morcrette, J.-J. (2019). Description and evaluation of the tropospheric aerosol scheme in the European Centre for Medium-Range Weather Forecasts (ECMWF) Integrated Forecasting System (IFS-AER, cycle 45R1). *Geosci. Model Dev.*, *12*(11), 4627–4659. doi: 10.5194/gmd-12-4627-2019

Riuttanen, L., Bister, M., Kerminen, V.-M., John, V. O., Sundström, A.-M., Maso, M. D., ... Kulmala, M. (2016). Observational evidence for aerosols increasing upper tropospheric humidity. *Atmos. Chem. Phys.*, *16*(22), 14331–14342. doi: 10.5194/acp-16-14331-2016

Samset, B. H., Stjern, C. W., Andrews, E., Kahn, R. A., Myhre, G., Schulz, M., & Schuster, G. L. (2018). Aerosol absorption: Progress towards global and regional constraints. *Curr. Clim. Change Rep.*, *4*(2), 65–83. doi: 10.1007/s40641-018-0091-4

Santee, M. L., Manney, G. L., Livesey, N. J., Schwartz, M. J., Neu, J. L., & Read, W. G. (2017). A comprehensive overview of the climatological composition of the Asian summer monsoon anticyclone based on 10 years of Aura Microwave Limb Sounder measurements. *J. Geophys. Res. Atmos.*, *122*, 5491–5514. doi: 10.1002/2016jd026408

Schumann, U., Bugliaro, L., Dörnbrack, A., Baumann, R., & Voigt, C. (2021). Aviation contrail cirrus and radiative forcing over europe during 6 months of covid-19. *Geophys. Res. Lett.*, *48*(8), e2021GL092771. doi: 10.1029/2021GL092771

Sindelarova, K., Granier, C., Bouarar, I., Guenther, A., Tilmes, S., Stavrakou, T., ... Knorr, W. (2014). Global data set of biogenic VOC emissions calculated by the MEGAN model over the last 30 years. *Atmos. Chem. Phys.*, *14*(17), 9317–9341. doi: 10.5194/acp-14-9317-2014

Stamnes, K., Tsay, S.-C., & Laszlo, I. (2000). *DISORT, a General-Purpose Fortran Program for Discrete-Ordinate-Method Radiative Transfer in*

Scattering and Emitting Layered Media: Documentation of Methodology. Tech. rep., Dept. of Physics and Engineering Physics, Stevens Institute of Technology, Hoboken, NJ 07030. (107pp., available at http://www.rtatmocn.com/disort/docs/DISORTReport1.1.pdf)

Stamnes, K., Tsay, S.-C., Wiscombe, W., & Jayaweera, K. (1988). Numerically stable algorithm for discrete-ordinate-method radiative transfer in multiple scattering and emitting layered media. *Appl. Opt.*, *27*(12), 2502–2509. doi: 10.1364/AO.27.002502

Stein, O., Schultz, M. G., Bouarar, I., Clark, H., Huijnen, V., Gaudel, A., ... Clerbaux, C. (2014). On the wintertime low bias of northern hemisphere carbon monoxide found in global model simulations. *Atmos. Chem. Phys.*, *14*(17), 9295–9316. doi: 10.5194/acp-14-9295-2014

Su, H., Jiang, J. H., Liu, X., Penner, J. E., Read, W. G., Massie, S., ... Santee, M. L. (2011). Observed increase of TTL temperature and water vapor in polluted clouds over Asia. *J. Climate*, *24*(11), 2728–2736. doi: 10.1175/2010jcli3749.1

Szopa, S., Naik, V., Adhikary, B., Artaxo, P., Berntsen, T., Collins, W. D., ... Zanis, P. (2021). Short-lived climate forcers. In V. Masson-Delmotte et al. (Eds.), *Climate change 2021: The physical science basis. contribution of working group i to the sixth assessment report of the intergovernmental panel on climate change* (p. n/a). Cambridge University Press. (In press)

Tegtmeier, S., Krüger, K., Birner, T., Davis, N. A., Davis, S., Fujiwara, M., ... Wright, J. S. (2022). Chapter 8: Tropical Tropopause Layer. In M. Fujiwara, G. Manney, L. Gray, & J. S. Wright (Eds.), *SPARC Report No. 10, WCRP Report 6/2021* (pp. 309–389). Munich: SPARC. doi: 10.17874/800DEE57D13

Theys, N., Van Roozendael, M., Hendrick, F., Fayt, C., Hermans, C., Baray, J.-L., ... De Mazière, M. (2007). Retrieval of stratospheric and tropospheric BrO columns from multi-axis DOAS measurements at Reunion Island (21°S, 56°E). *Atmos. Chem. Phys.*, *7*(18), 4733–4749. doi: 10.5194/acp-7-4733-2007

Thomason, L. W., & Vernier, J.-P. (2013). Improved SAGE II cloud/aerosol categorization and observations of the Asian tropopause aerosol layer: 1989–2005. *Atmos. Chem. Phys.*, *13*, 4605–4616. doi: 10.5194/acp-13-4605-2013

Tilmes, S., Hodzic, A., Emmons, L. K., Mills, M. J., Gettelman, A., Kinnison, D. E., ... Liu, X. (2019). Climate forcing and trends of organic aerosols in the Community Earth System Model (CESM2). *J. Adv. Model. Earth Syst.*, *11*(12), 4323–4351. doi: https://doi.org/10.1029/2019MS001827

Toohey, M., Krüger, K., Bittner, M., Timmreck, C., & Schmidt, H. (2014). The impact of volcanic aerosol on the Northern Hemisphere stratospheric polar vortex: mechanisms and sensitivity to forcing structure. *Atmos. Chem. Phys.*, *14*, 13063–13079. doi: 10.5194/acp-14-13063-2014

Twomey, S. (1977). The influence of pollution on the shortwave albedo of clouds. *J. Atmos. Sci.*, *34*(7), 1149–1152. doi: 10.1175/1520-0469(1977)034⟨1149:TIOPOT⟩2.0.CO;2

Vernier, J.-P., Fairlie, T. D., Deshler, T., Ratnam, M. V., Gadhavi, H., Kumar, B. S., ... Renard, J. B. (2017). BATAL: The Balloon measurement campaigns of the Asian Tropopause Aerosol Layer. *Bull. Am. Meteor. Soc.*, *99*, 955–973. doi: 10.1175/bams-d-17-0014.1

Vernier, J.-P., Fairlie, T. D., Natarajan, M., Wienhold, F. G., Bian, J., Martinsson, B. G., ... Bedka, K. M. (2015). Increase in upper tropospheric and lower stratospheric aerosol levels and its potential connection with Asian pollution. *J. Geophys. Res. Atmos.*, *120*, 1608–1619. doi: 10.1002/2014jd022372

Vernier, J.-P., Thomason, L. W., & Kar, J. (2011). CALIPSO detection of an Asian tropopause aerosol layer. *Geophys. Res. Lett.*, *38*, L07804. doi: 10.1029/2010gl046614

Vogel, B., Günther, G., Müller, R., Grooß, J.-U., Afchine, A., Bozem, H., ... Zahn,

A. (2016). Long-range transport pathways of tropospheric source gases originating in Asia into the northern lower stratosphere during the Asian monsoon season 2012. *Atmos. Chem. Phys.*, *16*(23), 15301–15325. doi: 10.5194/acp-16-15301-2016

Weigel, R., Mahnke, C., Baumgartner, M., Dragoneas, A., Vogel, B., Ploeger, F., ... Borrmann, S. (2021). In situ observation of new particle formation (npf) in the tropical tropopause layer of the 2017 asian monsoon anticyclone – part 1: Summary of stratoclim results. *Atmos. Chem. Phys.*, *21*(15), 11689–11722. doi: 10.5194/acp-21-11689-2021

Whitby, K. T. (1978). The physical characteristics of sulfur aerosols. *Atmos. Environ.*, *12*(1), 135–159. doi: 10.1016/0004-6981(78)90196-8

Wiedinmyer, C., Akagi, S. K., Yokelson, R. J., Emmons, L. K., Al-Saadi, J. A., Orlando, J. J., & Soja, A. J. (2011). The Fire INventory from NCAR (FINN): a high resolution global model to estimate the emissions from open burning. *Geosci. Model Dev.*, *4*(3), 625–641. Retrieved from `https://gmd.copernicus.org/articles/4/625/2011/` doi: 10.5194/gmd-4-625-2011

Wright, J. S., Fujiwara, M., Long, C., Anstey, J., Chabrillat, S., Compo, G. P., ... Zou, C.-Z. (2022). Chapter 2: Description of the Reanalysis Systems. In M. Fujiwara, G. Manney, L. Gray, & J. S. Wright (Eds.), *SPARC Report No. 10, WCRP Report 6/2021* (pp. 15–80). Munich: SPARC. doi: 10.17874/800DEE57D13

Yu, P., Rosenlof, K. H., Liu, S., Telg, H., Thornberry, T. D., Rollins, A. W., ... Gao, R.-S. (2017). Efficient transport of tropospheric aerosol into the stratosphere via the Asian summer monsoon anticyclone. *Proc. Natl. Acad. Sci. U.S.A.*, *114*, 6972–6977. doi: 10.1073/pnas.1701170114

Yu, P., Toon, O. B., Neely, R. R., Martinsson, B. G., & Brenninkmeijer, C. A. M. (2015). Composition and physical properties of the Asian Tropopause Aerosol Layer and the North American Tropospheric Aerosol Layer. *Geophys. Res. Lett.*, *42*, 2540–2546. doi: 10.1002/2015gl063181

Zhang, J., Wu, X., Bian, J., Xia, X., Bai, Z., Liu, Y., ... Lyu, D. (2020). Aerosol variations in the upper troposphere and lower stratosphere over the Tibetan Plateau. *Environ. Res. Lett.*, *15*(9), 094068. doi: 10.1088/1748-9326/ab9b43

Supporting Information for "Aerosol Effects on Clear-Sky Shortwave Heating in the Asian Monsoon Tropopause Layer"

Jie Gao[1], Yi Huang[2], Yiran Peng[1], and Jonathon S. Wright[1]

[1]Department of Earth System Science, Ministry of Education Key Laboratory for Earth System Modeling, and Institute for Global Change Studies, Tsinghua University, Beijing, China

[2]Department of Atmospheric and Oceanic Sciences, McGill University, Montreal, Quebec, Canada

Contents of this file

Introduction. This document summarizes technical details and previously published validation for MERRA-2 (Text S1; Table S1) and other reanalysis and forecast products (Text S2) as discussed in the main text. Nine supplementary figures are also included, mainly focusing on the species distributions in MERRA-2 and other products (Figs. S1–S5). Two alternative approaches to the calculation of ATAL radiative effects are also included (Figs. S6 and S7), along with two figures summarizing the magnitude of the ATAL effect relative to other factors as represented by MERRA-2 (Figs. S8 and S9).

Text S1: Additional details on MERRA-2. MERRA-2 is a state-of-the-art atmospheric reanalysis of the satellite era (1980–present) produced by the National Aeronautics and Space Administration (NASA) Global Modeling and Assimilation Office (GMAO). The model is run using version 5.12.4 of the Goddard Earth Observing System atmospheric model (GEOS-5) on a ∼50-km cubed sphere grid (data grid: 0.5°lat×0.625°lon) with 72 vertical levels and a model top at 0.01 hPa. The data assimilation takes place in two steps, with an incremental analysis update (Bloom et al., 1996) to apply adjustments calculated during an initial 3D-variational assimilation (additional details in Wright et al., 2022). Optical properties are largely taken from the Optical Properties of Aerosols and Clouds (OPAC) dataset (Hess et al., 1998) with some modifications. In particular, organic carbon from biomass burning is now partitioned directly to 'brown carbon' and dust optical properties are calculated assuming ellipsoid rather than spherical shapes (M. Chin, personal communication, 18 July 2020). With the exception of dust, aerosol hygroscopic growth is parameterized using separate functions of ambient relative humidity for each aerosol type (Chin et al., 2002; Colarco et al., 2014). Aerosol extinction coefficients increase with increasing relative humidity.

Aerosol data assimilation in MERRA-2 is restricted to measurements of vertically-integrated aerosol optical depth (AOD), and does not affect the composition and applies to all vertical levels simultaneously (Randles et al., 2017). Dust and sea salt emissions are wind-driven. Volcanic emissions are limited to an annually-repeating climatology of outgassing volcanoes, and do not account for volcanic eruptions that occurred after 2010. Anthropogenic aerosol emissions are taken from prescriptions developed for the AeroCom Phase II model intercomparison activity (Diehl et al., 2012), along with SO_2 from aircraft

and outgassing volcanoes. Emissions sources from AeroCom during our analyis period are fixed to values from 2006 (anthropogenic aerosols and aircraft SO_2) or 2007 (aerosol emissions from international shipping). Anthropogenic emissions of SO_2 from other sources are taken from the EDGARv4 database (Janssens-Maenhout, 2010, 2011). Emissions sources from EDGAR are fixed to values from 2005 (SO_2 from shipping; EDGARv4.1) or 2008 (anthropogenic SO_2; EDGARv4.2). Emissions of biogenic terpene are taken from the monthly climatology developed by Guenther et al. (1995), while emissions of dimethyl sulfide and methanesulfonic acid are taken from the monthly climatologies reported by Randerson et al. (2006).

Randles et al. (2017) evaluated the MERRA-2 aerosol analysis in terms of AOD and the aerosol direct radiative effects on clear-sky shortwave fluxes at the nominal top-of-atmosphere, surface, and net atmospheric convergence. Their results showed good agreement in both AOD and radiative effects validated against independent (i.e., unassimilated) measurements. Buchard et al. (2017) extended this validation to include aerosol absorption optical depth, ultraviolet aerosol index, and vertical aerosol profiles. Aerosol absorption optical depths and ultraviolet indices were in good agreement with values retrieved by the Ozone Monitoring Instrument (OMI), with evident improvement relative to aerosol analyses conducted using an earlier version of the GEOS-5 system (Buchard et al., 2015). Values of ultraviolet aerosol index tend to be biased low in areas with large values of brown carbon, which is not included in the MERRA-2 aerosol model and is also neglected in this study. MERRA-2 was also judged to perform well with respect to aerosol vertical profiles, although vertical gradients were often weaker than observed. Buchard et al. (2017) recommended that nearest-neighbor weighted combinations be used to improve

agreement with measured profiles. Since our analysis does not include direct comparison to measured profiles, we adopt a rough analogue to this approach by downgrading the spatial grid to 2.5°×2.5°, so that each profile is averaged across twenty grid cells (four in longitude by five in latitude).

Among available analysis and forecast products with an interactive ATAL (see section 4.2 in main text for examples), we choose to focus on MERRA-2 for two reasons. First, the MERRA-2 aerosol analysis is one of the few available aerosol analysis products to cover the entire period 2011–2020 using a consistent model and data assimilation system. This advantage in coverage provides a fuller characterization of the climatology and variability of the ATAL at interannual and intraseasonal scales, with the caveat that, as outlined above, most emissions sources do not vary from year to year during the 2011–2020 period. MERRA-2 for this period is thus not suitable for studying trends or variability linked to emissions (e.g., COVID-19), but is well suited to evaluating interannual variability driven by variations in the monsoon circulation and convective activity. Second, MERRA-2 is one of the few products to publish clear-sky radiative heating rate diagnostics along with interactive aerosol fields, which provide useful context for the offline radiative transfer calculations. These heating rates are calculated with reference to the aerosol fields during the incremental analysis update and are therefore consistent with ATAL composition and vertical structure as represented by the MERRA-2 products listed in Table S1.

Text S2: Other reanalysis products Several other recent reanalyses and operational forecasts of atmospheric composition are used to approximate uncertainty bounds for ATAL effects on clear-sky shortwave radiative heating (Table 2 in main text).

The first additional product, GEOS-FP (Forward Processing), is produced using a newer version of the same atmospheric model and data assimilation system as MERRA-2 (Lucchesi, 2018). Key developments relative to MERRA-2 include a finer horizontal model grid and the inclusion of nitrate and ammonium aerosols in the aerosol analysis. GEOS-FP uses the same emissions sources as MERRA-2: anthropogenic aerosol emissions and SO_2 from outgassing volcanoes are taken from the AeroCom Phase II archive (Diehl et al., 2012), while anthropogenic emissions of SO_2 and nitrate precursors from non-aircraft sources are taken from EDGARv4 (Janssens-Maenhout, 2010, 2011). We use the GEOS-FP analysis aerosol product on model levels for July–August 2020.

Two products from the Copernicus Atmosphere Monitoring Service (CAMS) and the European Centre for Medium-range Weather Forecasts (ECMWF) are considered, the CAMS ECMWF Atmospheric Composition Reanalysis 4 (CAMS-EAC4; Inness et al., 2019) for the full period 2011–2020 and the CAMS atmospheric composition forecast product (CAMS-FC; Rémy et al., 2019) for July–September 2020. Both CAMS-EAC4 and CAMS-FC use the Integrated Forecast System chemistry (IFS-CB05; Flemming et al., 2015) and aerosol (IFS-AER; Rémy et al., 2019) models. The CAMS-EAC4 product uses emissions from Monitoring Atmospheric Composition and Climate–CityZen (MACCity; Granier et al., 2011; Stein et al., 2014) for anthropogenic sources, Global Fire Assimilation System (GFAS) version 1.2 (Kaiser et al., 2012) for biomass burning, Model of Emissions of Gases and Aerosols from Nature (MEGAN) simulations for biogenic emissions (Sindelarova et al., 2014), and a climatology of volcanic outgassing. Unlike GEOS-FP and CAMS-EAC4, we use forecast rather than analysis products from CAMS-FC. CAMS-FC has a finer horizontal resolution and additional vertical levels relative to

CAMS-EAC4, includes nitrate and ammonium aerosols where CAMS-EAC4 does not, and implements a more realistic relationship between sulfur dioxide (from the chemistry scheme) and sulfate aerosols (from the aerosol scheme). Emissions sources are similar, but with version 1.2 of GFAS replaced by version 1.4. This and other differences between CAMS-EAC4 and CAMS-FC have been documented in detail by Rémy et al. (2019).

The final additional dataset is a set of 10-day forecast products generated by the National Center for Atmospheric Research (NCAR) Atmospheric Chemistry Observations & Modeling group using version 6 of the Whole Atmosphere Community Climate Model (WACCM; Gettelman et al., 2019). Interactive chemistry is based on the Model for OZone and Related chemical Tracers for the Troposphere, Stratosphere, Mesosphere, and Lower Thermosphere (MOZART-TSLMT; Emmons et al., 2020) and aerosols are simulated using the Modal Aerosol Module (MAM4; Liu et al., 2016; Tilmes et al., 2019). Anthropogenic emissions are the same as in the CAMS products (MACCity), while fire emissions are taken from the Fire INventory from NCAR (FINN; Wiedinmyer et al., 2011). Volcanic emissions are based on a time-mean climatology for 1850–2014 that includes both outgassing and eruptive emissions (Neely III & Schmidt, 2016). No observations are assimilated in the WACCM forecasts; however, the model is driven by meteorological fields taken from the GEOS-FP product described above. WACCM forecasts are used for July–September 2020.

Given data availability limitations and model version changes, the forecast and analysis products GEOS-FP, CAMS 46r1FC, and WACCM are used only for comparison with MERRA-2 during the year 2020 (section 4.2 in main text).

References

Bloom, S. C., Takacs, L. L., da Silva, A. M., & Ledvina, D. (1996). Data assimilation using incremental analysis updates. *Mon. Wea. Rev.*, *124*, 1256–1271. doi: 10.1175/1520-0493(1996)124⟨1256:DAUIAU⟩2.0.CO;2

Buchard, V., da Silva, A. M., Colarco, P. R., Darmenov, A., Randles, C. A., Govindaraju, R., ... Spurr, R. (2015). Using the OMI aerosol index and absorption aerosol optical depth to evaluate the NASA MERRA Aerosol Reanalysis. *Atmos. Chem. Phys.*, *15*(10), 5743–5760. doi: 10.5194/acp-15-5743-2015

Buchard, V., Randles, C. A., Silva, A. M. d., Darmenov, A., Colarco, P. R., Govindaraju, R., ... Yu, H. (2017). The MERRA-2 Aerosol Reanalysis, 1980 Onward. Part II: Evaluation and Case Studies. *J. Climate*, *30*(17), 6851–6872. doi: 10.1175/jcli-d-16-0613.1

Chin, M., Ginoux, P., Kinne, S., Torres, O., Holben, B. N., Duncan, B. N., ... Nakajima, T. (2002). Tropospheric aerosol optical thickness from the GOCART model and comparisons with satellite and sun photometer measurements. *J. Atmos. Sci.*, *59*, 461–483. doi: 10.1175/1520-0469(2002)059⟨0461:TAOTFT⟩2.0.CO;2

Colarco, P. R., Nowottnick, E. P., Randles, C. A., Yi, B., Yang, P., Kim, K.-M., ... Bardeen, C. G. (2014). Impact of radiatively interactive dust aerosols in the NASA GEOS-5 climate model: Sensitivity to dust particle shape and refractive index. *J. Geophys. Res. Atmos.*, *119*(2), 753–786. doi: 10.1002/2013jd020046

Diehl, T., Heil, A., Chin, M., Pan, X., Streets, D., Schultz, M., & Kinne, S. (2012). Anthropogenic, biomass burning, and volcanic emissions of black carbon, organic carbon, and SO_2 from 1980 to 2010 for hindcast model experiments. *Atmos. Chem.*

Phys. Discuss., *12*, 24895–24954. doi: 10.5194/acpd-12-24895-2012

Emmons, L. K., Schwantes, R. H., Orlando, J. J., Tyndall, G., Kinnison, D., Lamarque, J.-F., ... Pétron, G. (2020). The chemistry mechanism in the Community Earth System Model Version 2 (CESM2). *J. Adv. Model. Earth Syst.*, *12*(4), e2019MS001882. doi: 10.1029/2019MS001882

Flemming, J., Huijnen, V., Arteta, J., Bechtold, P., Beljaars, A., Blechschmidt, A.-M., ... Tsikerdekis, A. (2015). Tropospheric chemistry in the Integrated Forecasting System of ECMWF. *Geosci. Model Dev.*, *8*(4), 975–1003. Retrieved from `https://gmd.copernicus.org/articles/8/975/2015/` doi: 10.5194/gmd-8-975-2015

Gettelman, A., Mills, M. J., Kinnison, D. E., Garcia, R. R., Smith, A. K., Marsh, D. R., ... Randel, W. J. (2019). The Whole Atmosphere Community Climate Model Version 6 (WACCM6). *J. Geophys. Res. Atmos.*, *124*(23), 12380–12403. doi: 10.1029/2019JD030943

Global Modeling and Assimilation Office. (2015a). *MERRA-2 inst3_3d_aer_Nv: 3d, 3-Hourly, Instantaneous, Model-Level, ssimilation, Aerosol Mixing Ratio V5.12.4* [dataset]. NASA Goddard Earth Sciences Data and Information Services Center. doi: 10.5067/LTVB4GPCOTK2

Global Modeling and Assimilation Office. (2015b). *MERRA-2 inst3_3d_asm_Nv: 3d, 3-Hourly, Instantaneous, Model-Level, Assimilation, Assimilated Meteorological Fields V5.12.4* [dataset]. NASA Goddard Earth Sciences Data and Information Services Center. doi: 10.5067/WWQSXQ8IVFW8

Global Modeling and Assimilation Office. (2015c). *MERRA-2 tavg1_2d_rad_Nx: 2d, 1-Hourly, Time-Averaged, Single-Level, Assimilation, Radiation Diagnostics V5.12.4*

[dataset]. NASA Goddard Earth Sciences Data and Information Services Center. doi: 10.5067/Q9QMY5PBNV1T

Global Modeling and Assimilation Office. (2015d). *MERRA-2 tavg3_3d_rad_Nv: 3d, 3-Hourly, Time-Averaged, Model-Level, Assimilation, Radiation Diagnostics V5.12.4* [dataset]. NASA Goddard Earth Sciences Data and Information Services Center. doi: 10.5067/7GFQKO1T43RW

Granier, C., Bessagnet, B., Bond, T., D'Angiola, A., Gon, H. D. v. d., Frost, G. J., ... Vuuren, D. P. v. (2011). Evolution of anthropogenic and biomass burning emissions of air pollutants at global and regional scales during the 1980–2010 period. *Clim. Change*, *109*(1-2), 163. doi: 10.1007/s10584-011-0154-1

Guenther, A., Hewitt, C. N., Erickson, D., Fall, R., Geron, C., Graedel, T., ... Zimmerman, P. (1995). A global model of natural volatile organic compound emissions. *J. Geophys. Res. Atmos.*, *100*(D5), 8873–8892. doi: 10.1029/94JD02950

Hess, M., Koepke, P., & Schult, I. (1998). Optical Properties of Aerosols and Clouds: The software package OPAC. *Bull. Am. Meteor. Soc.*, *79*, 831–844. doi: 10.1175/1520-0477(1998)079⟨0831:opoaac⟩2.0.co;2

Inness, A., Ades, M., Agustí-Panareda, A., Barré, J., Benedictow, A., Blechschmidt, A.-M., ... Suttie, M. (2019). The CAMS reanalysis of atmospheric composition. *Atmos. Chem. Phys.*, *19*(6), 3515–3556. doi: 10.5194/acp-19-3515-2019

Janssens-Maenhout, G. (2010). *EDGARv4.1 Emission Maps* [dataset]. European Commission, Joint Research Centre (JRC). (http://data.europa.eu/89h/jrc-edgar-emissionmapsv41)

Janssens-Maenhout, G. (2011). *EDGARv4.2 Emission Maps* [dataset]. European

Commission, Joint Research Centre (JRC). (http://data.europa.eu/89h/jrc-edgar-emissionmapsv42)

Kaiser, J. W., Heil, A., Andreae, M. O., Benedetti, A., Chubarova, N., Jones, L., ... van der Werf, G. R. (2012). Biomass burning emissions estimated with a global fire assimilation system based on observed fire radiative power. *Biogeosciences*, *9*(1), 527–554. doi: 10.5194/bg-9-527-2012

Liu, X., Ma, P.-L., Wang, H., Tilmes, S., Singh, B., Easter, R. C., ... Rasch, P. J. (2016). Description and evaluation of a new four-mode version of the Modal Aerosol Module (MAM4) within version 5.3 of the Community Atmosphere Model. *Geosci. Model Dev.*, *9*(2), 505–522. doi: 10.5194/gmd-9-505-2016

Lucchesi, R. (2018). *File specification for GEOS-5 FP.* GMAO Office Note No. 4 (version 1.2), Greenbelt, Maryland. (62 pp., available at http://gmao.gsfc.nasa.gov/pubs/office_notes)

Neely III, R., & Schmidt, A. (2016). *Volcaneesm: Global volcanic sulphur dioxide (so2) emissions database from 1850 to present - version 1.0* [dataset]. NERC Centre for Environmental Data Analysis (CEDA). Retrieved from `https://catalogue.ceda.ac.uk/uuid/a8a7e52b299a46c9b09d8e56b283d385` doi: 10.5285/76EBDC0B-0EED-4F70-B89E-55E606BCD568

Randerson, J. T., Liu, H., Flanner, M. G., Chambers, S. D., Jin, Y., Hess, P. G., ... Zender, C. S. (2006). The impact of boreal forest fire on climate warming. *Science*, *314*(5802), 1130–1132. doi: 10.1126/science.1132075

Randles, C. A., Silva, A. M. d., Buchard, V., Colarco, P. R., Darmenov, A., Govindaraju, R., ... Flynn, C. J. (2017). The MERRA-2 Aerosol Reanalysis, 1980 onward. Part

I: System description and data assimilation evaluation. *J. Climate*, *30*, 6823–6850. doi: 10.1175/jcli-d-16-0609.1

Rémy, S., Kipling, Z., Flemming, J., Boucher, O., Nabat, P., Michou, M., ... Morcrette, J.-J. (2019). Description and evaluation of the tropospheric aerosol scheme in the European Centre for Medium-Range Weather Forecasts (ECMWF) Integrated Forecasting System (IFS-AER, cycle 45R1). *Geosci. Model Dev.*, *12*(11), 4627–4659. doi: 10.5194/gmd-12-4627-2019

Sindelarova, K., Granier, C., Bouarar, I., Guenther, A., Tilmes, S., Stavrakou, T., ... Knorr, W. (2014). Global data set of biogenic VOC emissions calculated by the MEGAN model over the last 30 years. *Atmos. Chem. Phys.*, *14*(17), 9317–9341. doi: 10.5194/acp-14-9317-2014

Stein, O., Schultz, M. G., Bouarar, I., Clark, H., Huijnen, V., Gaudel, A., ... Clerbaux, C. (2014). On the wintertime low bias of northern hemisphere carbon monoxide found in global model simulations. *Atmos. Chem. Phys.*, *14*(17), 9295–9316. doi: 10.5194/acp-14-9295-2014

Tilmes, S., Hodzic, A., Emmons, L. K., Mills, M. J., Gettelman, A., Kinnison, D. E., ... Liu, X. (2019). Climate forcing and trends of organic aerosols in the Community Earth System Model (CESM2). *J. Adv. Model. Earth Syst.*, *11*(12), 4323–4351. doi: https://doi.org/10.1029/2019MS001827

Wiedinmyer, C., Akagi, S. K., Yokelson, R. J., Emmons, L. K., Al-Saadi, J. A., Orlando, J. J., & Soja, A. J. (2011). The Fire INventory from NCAR (FINN): a high resolution global model to estimate the emissions from open burning. *Geosci. Model Dev.*, *4*(3), 625–641. Retrieved from `https://gmd.copernicus.org/articles/4/625/`

2011/ doi: 10.5194/gmd-4-625-2011

Wright, J. S., Fujiwara, M., Long, C., Anstey, J., Chabrillat, S., Compo, G. P., ... Zou, C.-Z. (2022). Chapter 2: Description of the Reanalysis Systems. In M. Fujiwara, G. Manney, L. Gray, & J. S. Wright (Eds.), *SPARC Report No. 10, WCRP Report 6/2021* (pp. 15–80). Munich: SPARC. doi: 10.17874/800DEE57D13

Table S1. MERRA-2 data collections used in this work.

Name	Variables	Time	Citation
M2I3NVAER	BC, OC, SO_4, dust	daily	Global Modeling and Assimilation Office (2015a)
M2I3NVASM	T, q, O_3, z, p	daily	Global Modeling and Assimilation Office (2015b)
M2T3NVRAD	SWHR, SWHRCLR	daily, 06Z	Global Modeling and Assimilation Office (2015d)
M2T1NXRAD	surface albedo	hourly	Global Modeling and Assimilation Office (2015c)

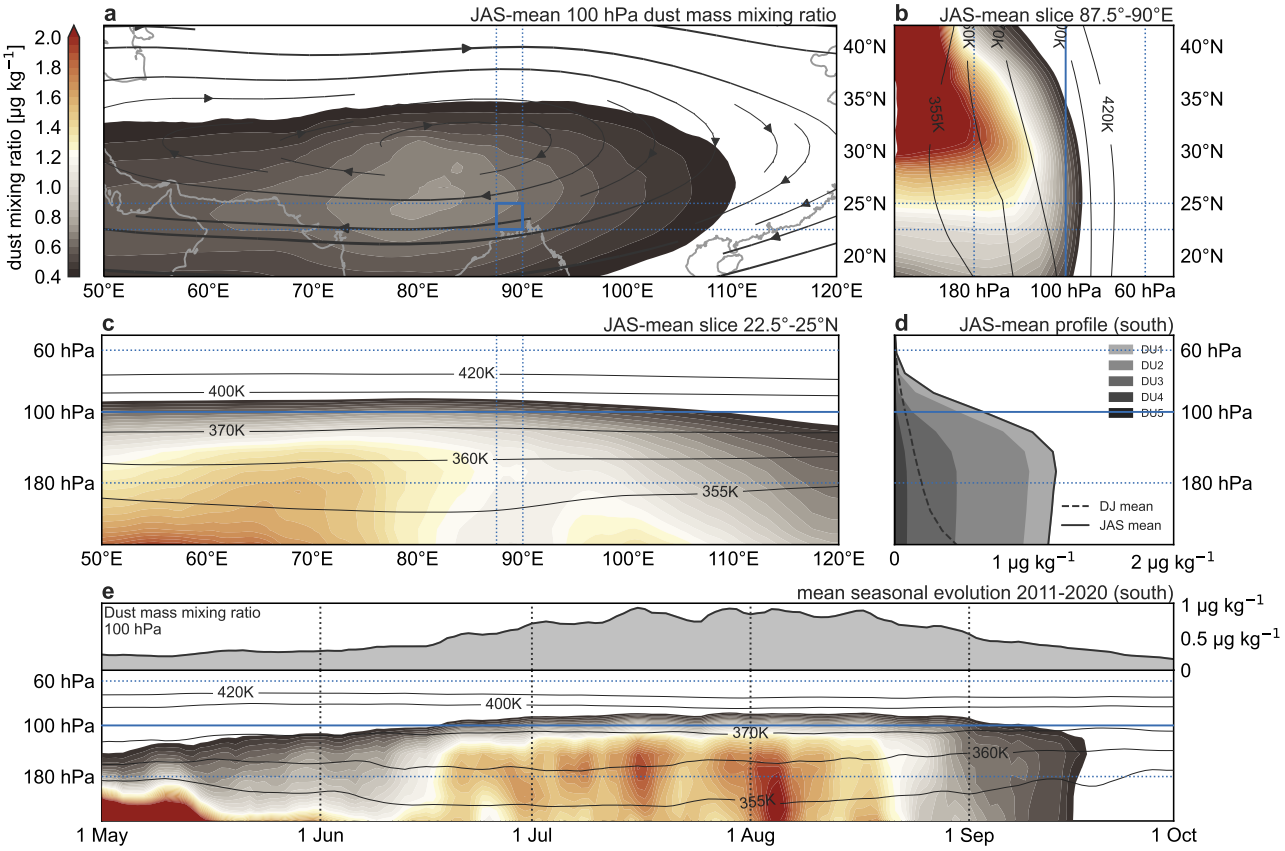

Figure S1. Distributions of mineral dust mass mixing ratios based on the MERRA-2 aerosol reanalysis (a) as a function of latitude and longitude on the 100 hPa isobaric surface, (b) as a function of latitude and pressure along the 87.5°E–90°E longitude band, (c) as a function of longitude and pressure along the 22.5°N–25°N latitude band, and (d) as an area-average profile within 87.5°E–90°E and 22.5°N–25°N for July, August, and September 2011–2020. (e) Mean evolution of dust profile (lower panel) and partial column (vertically-integrated over 180–60 hPa; upper panel) within 87.5°E–90°E and 22.5°N–25°N from 1 May to 30 September 2011–2020. Streamlines in (a) show the upper-level anticyclone at 100 hPa based on MERRA-2. Contours in (b), (c), and (e) show potential temperature surfaces spanning the upper troposphere and lower stratosphere. Shaded regions in (d) and (e) illustrate the relative abundances of different size bins of dust, listed from small (DU1, < 1 μm) to large (DU5; 6–10 μm).

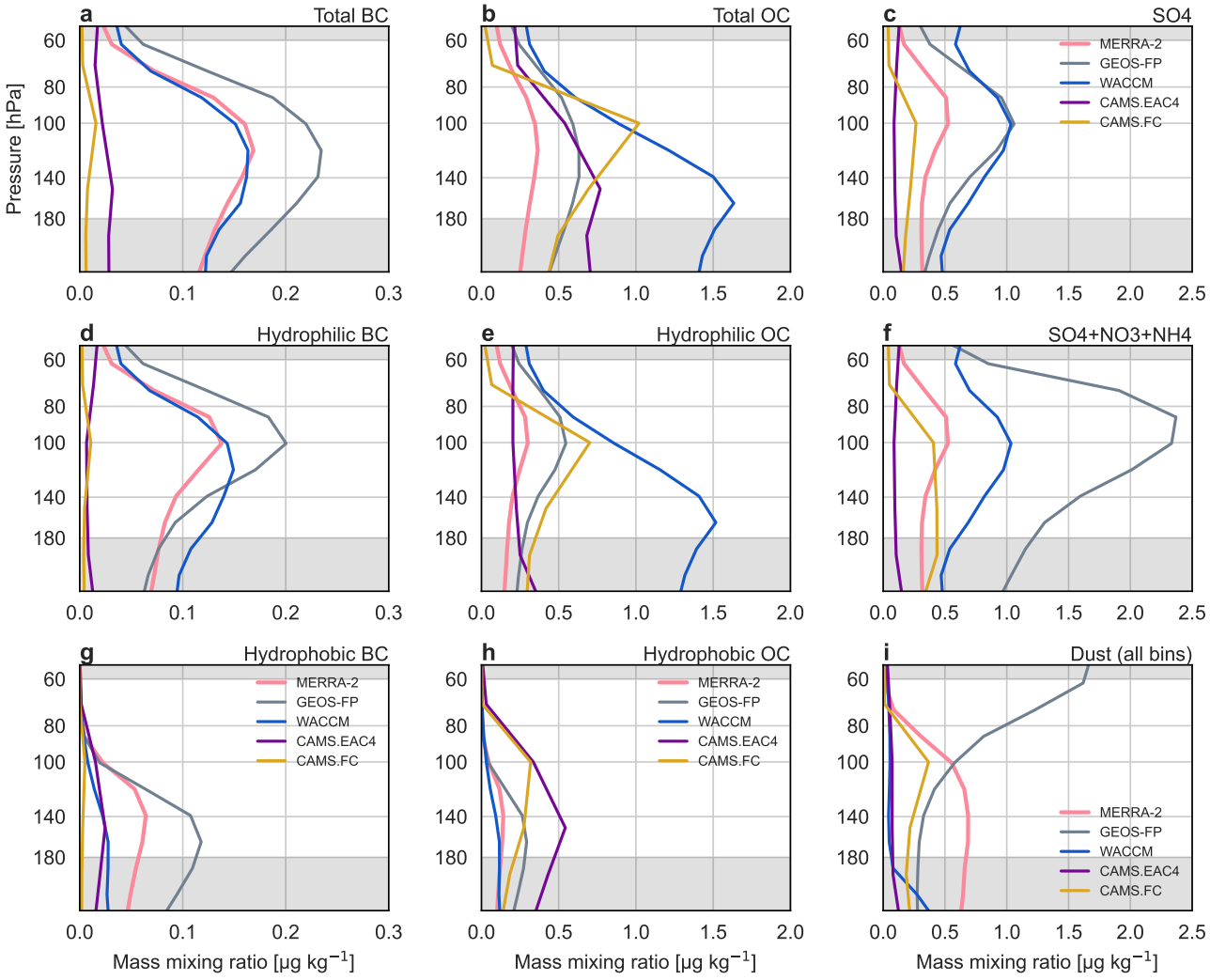

Figure S2. Vertical profiles of (a) total black carbon, (b) total organic carbon, (c) sulfate aerosol, (d) hydrophilic black carbon, (e) hydrophilic organic carbon, (f) sulfate + nitrate + ammonium aerosol, (g) hydrophobic black carbon, (h) hydrophobic organic carbon, and (i) mineral dust from all size bins based on the MERRA-2 (pink), GEOS-FP (grey), WACCM (blue), CAMS-EAC4 (purple), CAMS-FC (yellow) aerosol analysis (MERRA-2, GEOS-FP, and CAMS-EAC4) and forecast (WACCM and CAMS-FC) products. Grey shading indicates the bounds of the ATAL layer (60–180 hPa).

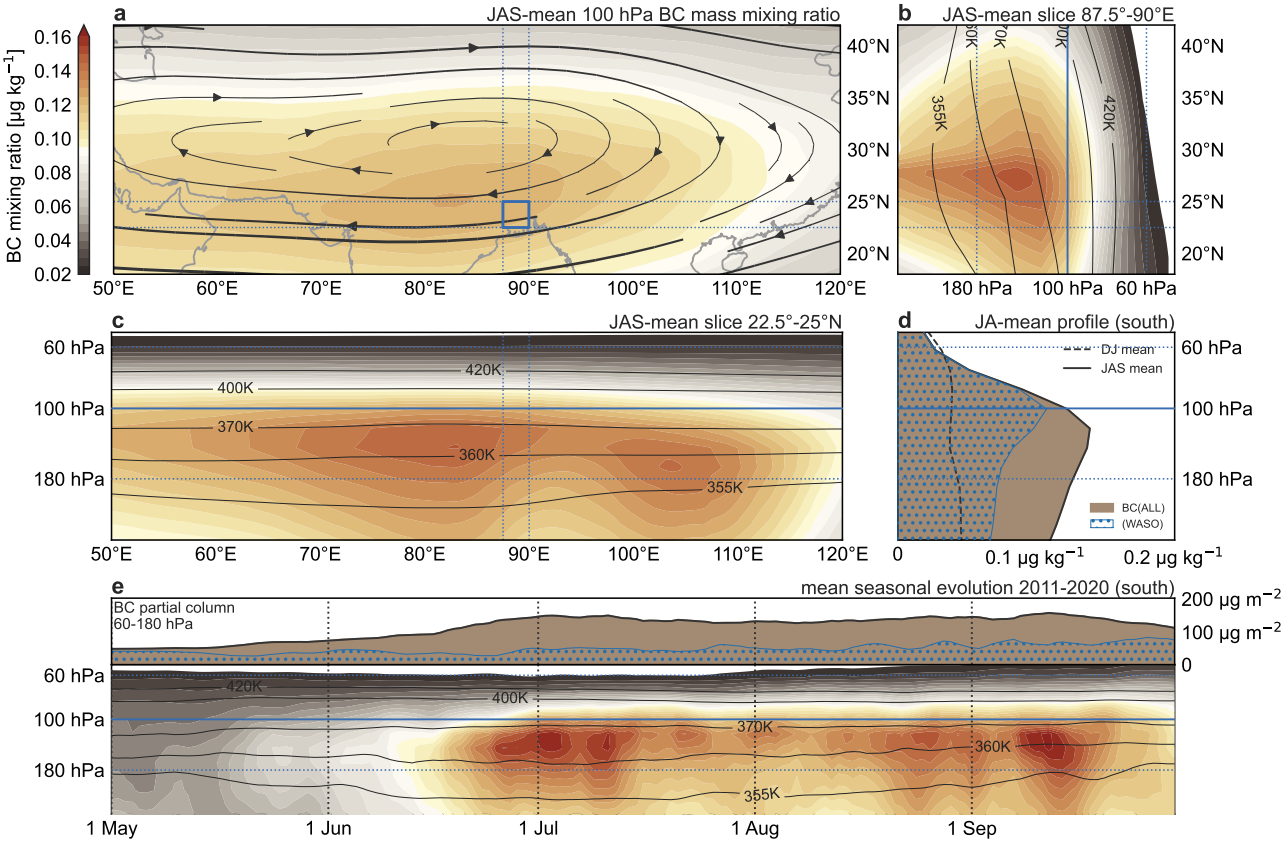

Figure S3. As in Fig. S1, but for black carbon (BC).

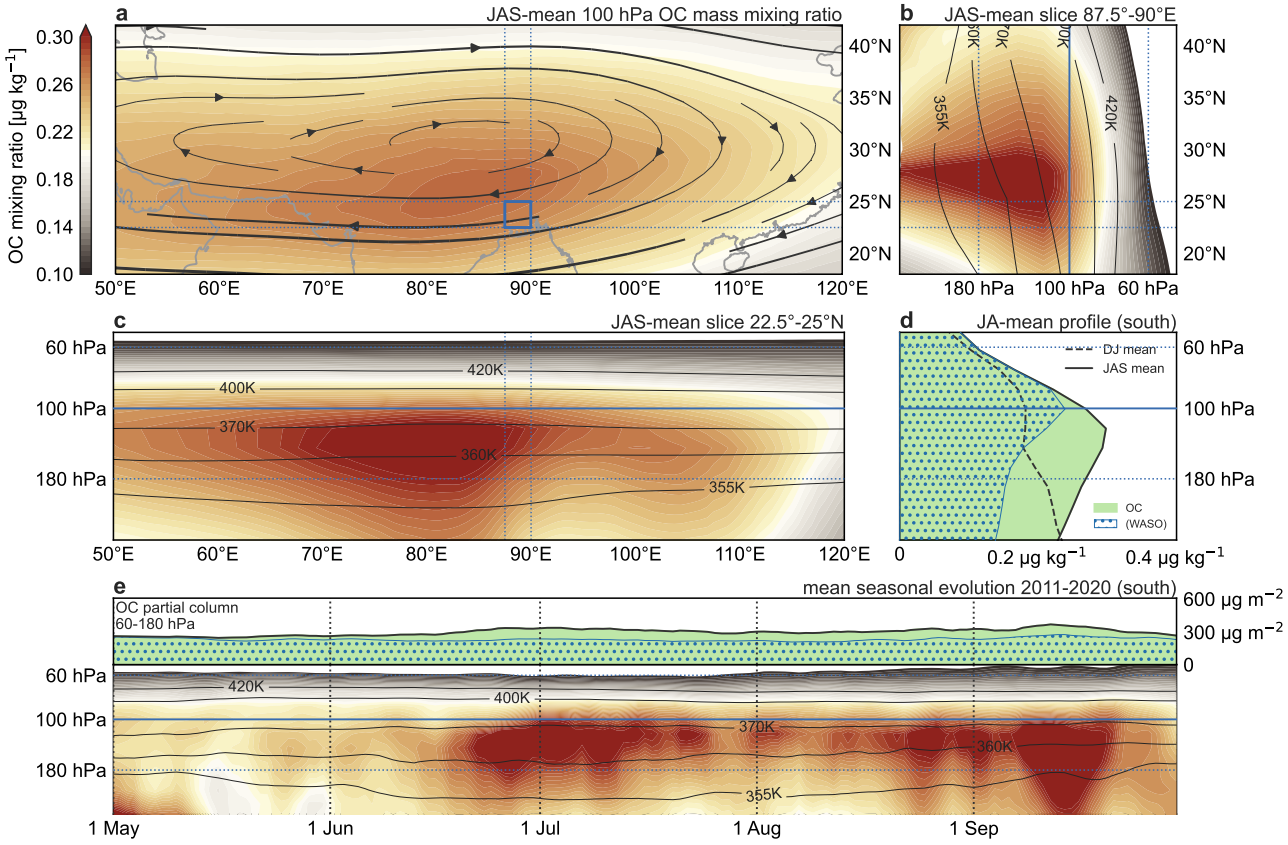

Figure S4. As in Fig. S1, but for organic carbon (OC).

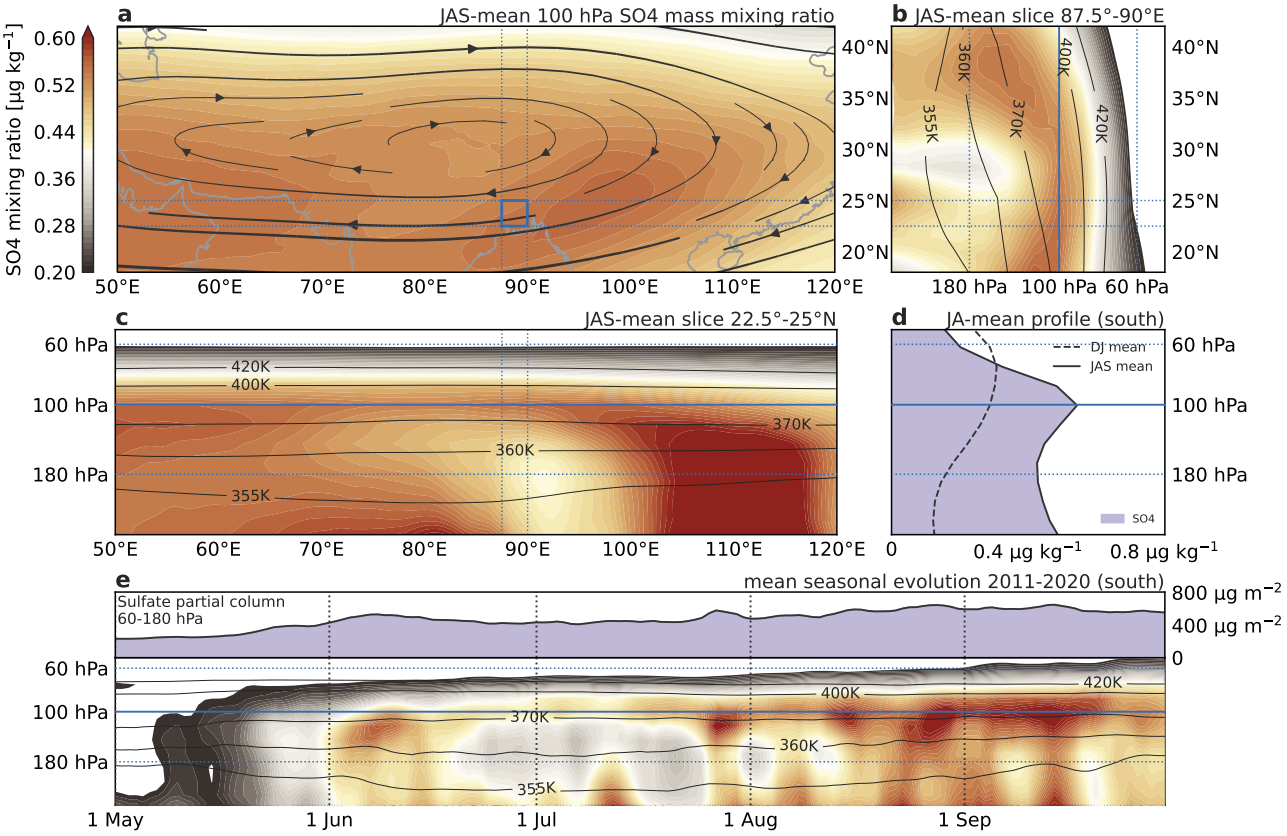

Figure S5. As in Fig. S1, but for sulfate.

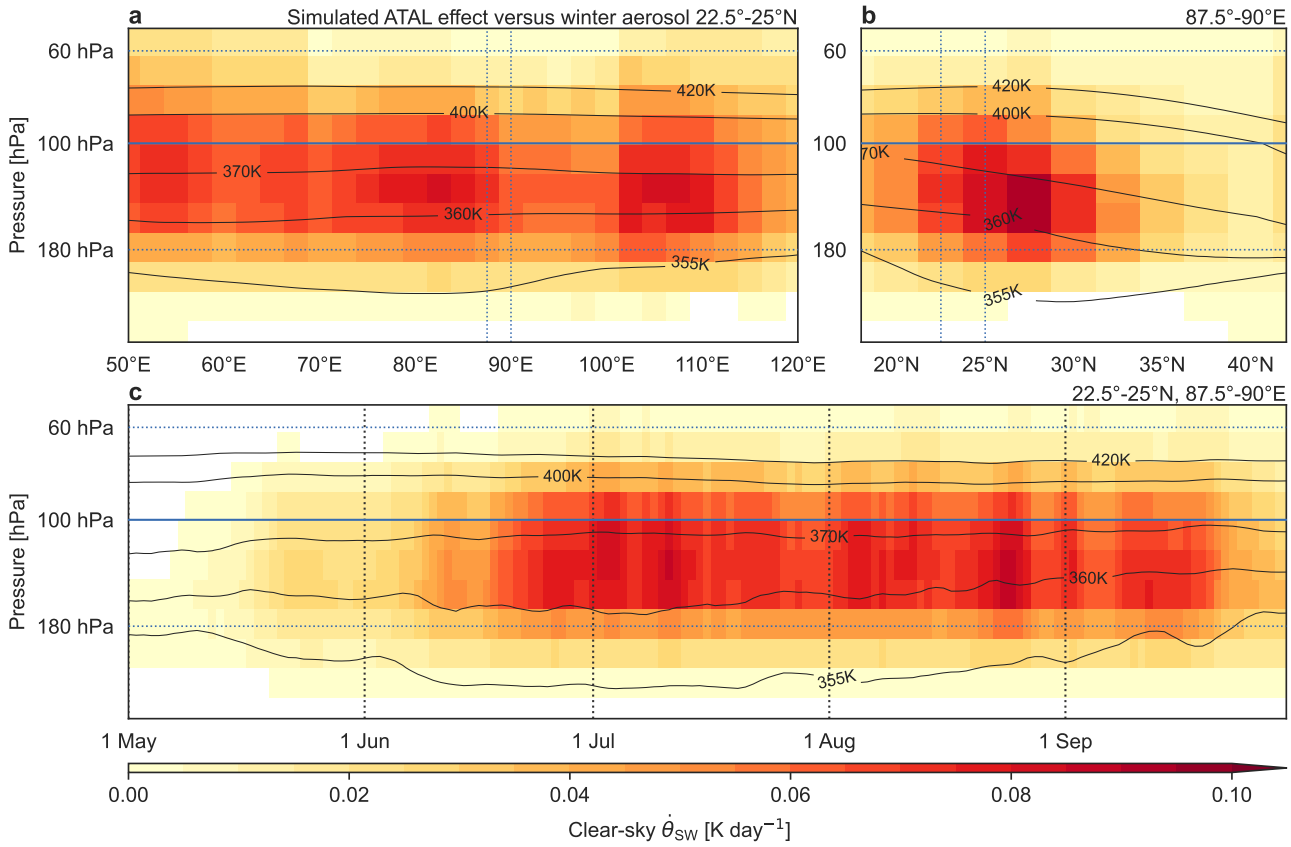

Figure S6. Variations in (a) longitude, (b) latitude, and (c) day-of-year for the simulated ATAL effect relative to an invariant representative winter-mean (December 2007 –January 2008) aerosol profile from MERRA-2 for the core region (22.5°N–25°N, 87.5°E–90°N). Panel c corresponds to Fig. 4b in the main text but with the winter-mean profile used as the reference state in place of the no-aerosol profile. Other radiatively active species are specified for both the winter-mean and ATAL simulations as July–August 2011–2020 means for each location in panels a–b and for each day of year averaged over 2011–2020 in the core region in panel c. Heating rates have been divided by the Exner function to convert $\partial T/\partial t$ to $\dot{\theta}$ for ease of comparison to potential temperature contours.

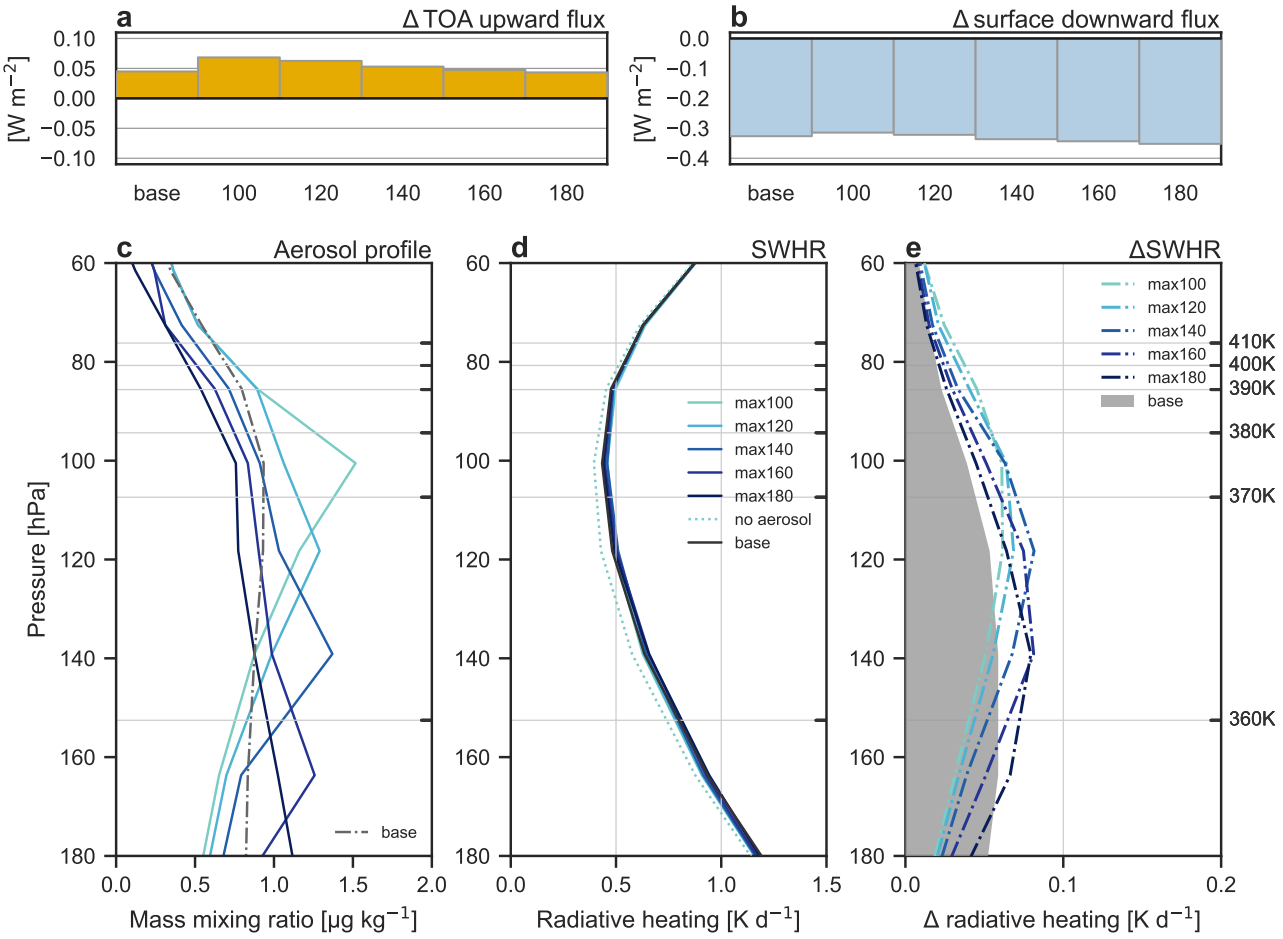

Figure S7. Variations in (a) top-of-atmosphere upward shortwave flux anomalies, (b) surface downward shortwave flux anomalies, (c) vertical profiles of aerosol mass mixing ratio, (d) shortwave radiative heating, and (e) aerosol effects on shortwave radiative heating relative to the no-aerosol case as a function of the height of the peak ATAL aerosol concentration. The vertically integrated mass and composition of ATAL aerosol are held fixed in all simulations while peak heights are varied from 100 hPa to 180 hPa. Heating rate profiles are calculated assuming a solar zenith angle of zero and a surface albedo of 0.15; TOA and surface fluxes are daily-mean values for solar parameters valid on 15 August at Dhaka.

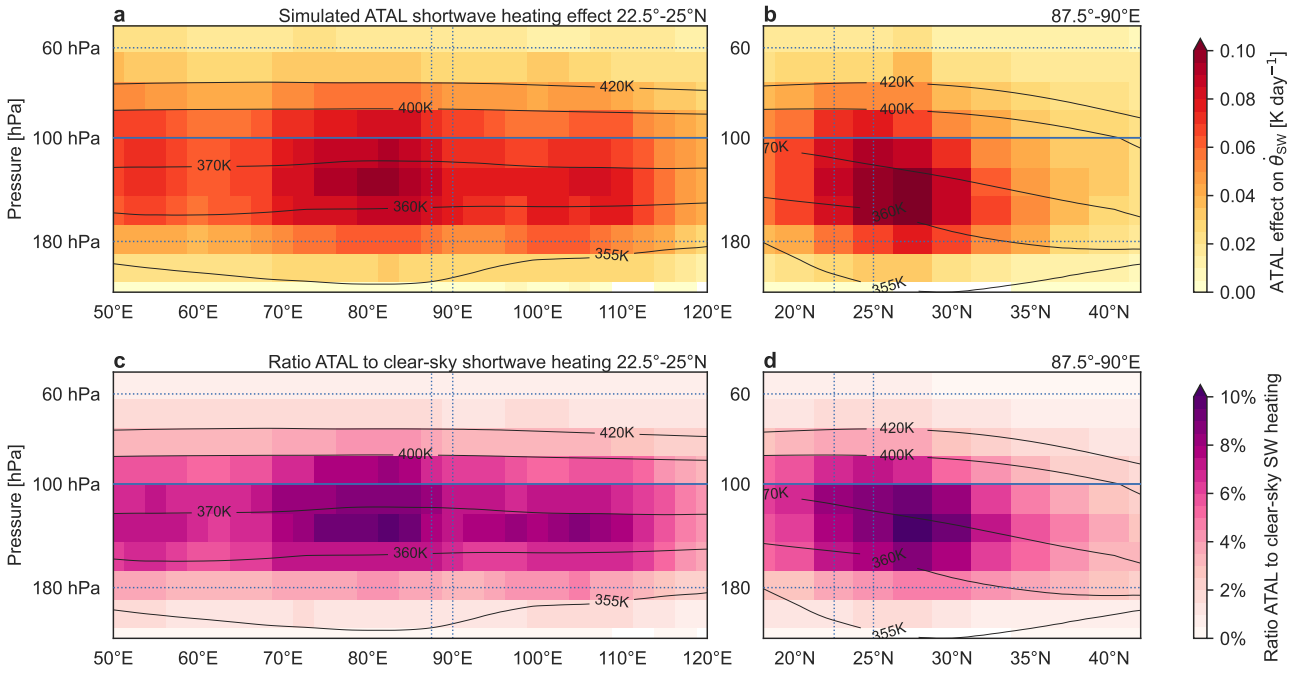

Figure S8. The mean ATAL shortwave heating effect as a function of (a) longitude (50°E–120°E meridionally averaged over 22.5°N–25°N) and latitude (18°N–42°N zonally averaged over 87.5°E–90°E). Lower panels show the ratio of the ATAL effects relative to (c)–(d) clear-sky shortwave heating from libRadtran. Inputs to libRadtran are based on July–September 2011–2020 means assuming a solar zenith angle of 0° and a surface albedo of 0.15. Heating rates in panels a–b have been divided by the Exner function to convert $\partial T/\partial t$ to $\dot{\theta}$ for ease of comparison to potential temperature contours.

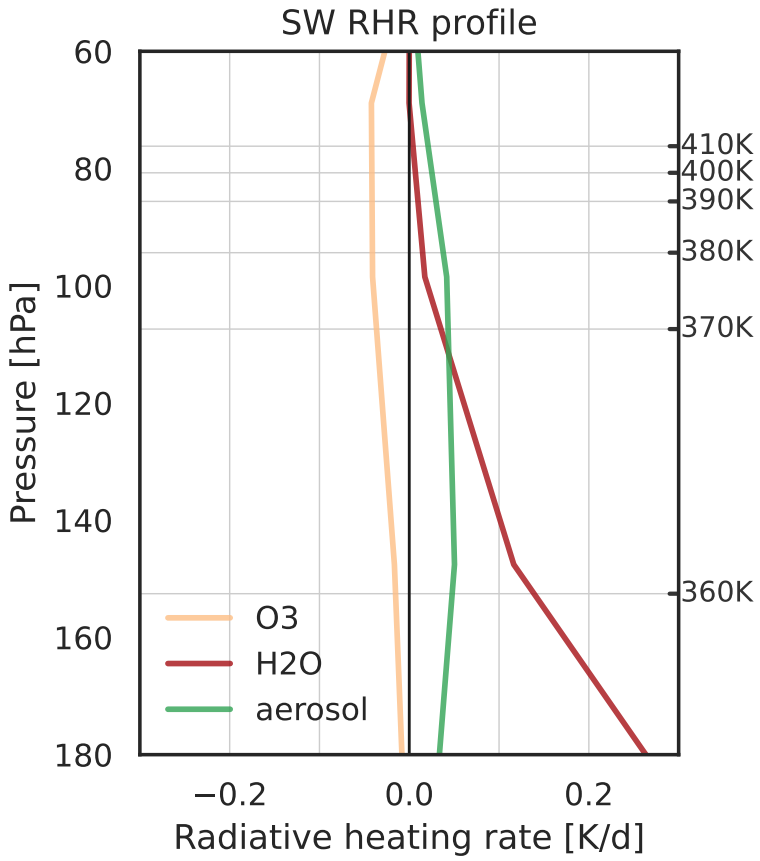

Figure S9. Vertical profiles of effects on clear-sky shortwave heating from ozone (yellow), water vapor (magenta), and aerosol (green) based on the July–August 2011–2020 mean for the core analysis region (22.5°N–25°N, 87.5°E–90°E) in MERRA-2. All effects are calculated by offline radiative transfer calculations assuming a solar zenith angle of 0° and a surface albedo of 0.15. The aerosol effect is calculated relative to the no-aerosol baseline; the ozone and water vapor effects are calculated for monsoon anomalies relative to zonal means within the 22.5°N–25°N latitude band. Heating rates are given as temperature tendency ($\partial T/\partial t$).